THESIS

SIMULATING THE EFFECTS OF COATED ICE NUCLEI IN THE FORMATION OF THIN ICE CLOUDS IN THE HIGH ARCTIC USING RAMS

Submitted by

Robert Seigel

Department of Atmospheric Science

In partial fulfillment of the requirements

For the Degree of Master of Science

Colorado State University

Fort Collins, Colorado

Spring 2010

COLORADO STATE UNIVERSITY

December 4, 2009

WE HEREBY RECOMMEND THAT THE THESIS PREPARED UNDER OUR SUPERVISION BY ROBERT SEIGEL ENTITLED SIMULATING THE EFFECTS OF COATED ICE NUCLEI IN THE FORMATION OF THIN ICE CLOUDS IN THE HIGH ARCTIC USING RAMS BE ACCEPTED AS FULFILLING IN PART REQUIREMENTS FOR THE DEGREE OF MASTER OF SCIENCE.

Committee on Graduate work

Steven Fassnacht

Gustavo Carrió

Advisor: William Cotton

Co-Advisor: Graeme Stephens

Department Head: Richard Johnson

ABSTRACT OF THESIS

SIMULATING THE EFFECTS OF COATED ICE NUCLEI IN THE FORMATION OF THIN ICE CLOUDS IN THE HIGH ARCTIC USING RAMS

The Polar regions are an integral part of Earth's energy budget, however they are poorly understood mainly due to their remoteness and lack of observations. The recent launch of two successful satellites, CloudSat and CALIPSO, into the A-Train constellation are providing excellent insight into wintertime clouds and precipitation at the Poles. One distinguishable characteristic seen from satellite data during Arctic winter and spring is an optically thin cloud containing ice crystals large enough to precipitate out. These "thin ice clouds" (TIC) occur in regions affected by anthropogenic pollution. It is hypothesized that the anthropogenic pollution, likely sulfuric acid, coat the available ice forming nuclei (IN) and render them inactive for forming ice crystals. Therefore, the effective IN concentrations are reduced in these regions and there is less competition for the same available moisture leading to the formation of relatively small concentrations of large ice crystals. The ice crystals grow large enough for sedimentation, which dehydrates the Arctic atmosphere.

We use Colorado State University's Regional Atmospheric Modeling System (RAMS) configured as a cloud resolving high-resolution model (CRM) with horizontal grid-spacing of 100m to simulate these TIC's. Varying ice nuclei (IN) concentrations from 5 L^{-1} to 100L^{-1} are used to simulate the effects of the acidic coating, whereby the low IN concentration represents the IN particles containing the acidic coating. Results show no concrete evidence in support of the hypothesis. Therefore, a sensitivity experiment is conducted to identify the environmental conditions that maximize the production of TIC's. Results indicate that an increase in both the temperature and supersaturation relative to observations provide a better environment for the production of TIC's.

Robert Seigel
Department of Atmospheric Science
Colorado State University
Fort Collins, CO 80523
Spring 2010

ACKNOWLEDGEMENTS

I would like to thank both Dr. William Cotton and Dr. Graeme Stephens for giving me the opportunity to study under with them in the Colorado State Atmospheric Science department. I am also grateful to Dr. Gustavo Carrió for his tremendous support and advice. All the members of the Cotton project group and Stephens research group helped this project enormously with instruction and advice. Special thanks to Noel Bryan, Brenda Thompson, Steve Saleeby, Dan Ward, Will Cheng, Natalie Tourville, Chris O'Dell, Matt Rogers, John Haines, and Norm Wood for inspiration and for always being happy to help a grad student. This project was supported by a fellowship from the National Aeronautics and Space Administration (NASA) under grant NNX07AR11G. I would also like to give my gratitude to Dr. Steven Fassnacht for being a member of my committee.

Many people freely provided me with data for this project. I would like to recognize Dr. Jean-Pierre Blanchet (University of Quebec, Montreal) and Rodrigo Munoz Alpizar (UQAM) for aiding me in this capacity. Finally, I am greatly indebted to my family for their unending love and support. Thanks especially to Jenna for her understanding and motivation during this experience.

TABLE OF CONTENTS

CHAPTER 1

INTRODUCTION

In recent years, there has been a drastic increase in the number of scientists studying Earth's climate. While our climate is extremely complex and subject to change, the Arctic is a region of particular importance and vulnerability to global climate change (IPCC 1990). Clouds play an important role in the Arctic surface energy budget, especially during winter, as they are the main source of downward longwave radiation. Atmospheric aerosols can act as an additional source of cloud condensation nuclei (CCN) and ice nuclei (IN) that can affect the Arctic clouds. An increase in either CCN or IN can affect the clouds by increasing hydrometeor number concentrations and reducing the overall hydrometeor diameters. These microphysical changes increases cloud residence time and therefore affect the surface energy budget by increasing the downward longwave radiation (Carrío et al. 2005). Since the late 1960's, the Arctic near-surface warming has increased by approximately twice that of the global average (MacBean 2004) and annual mean sea ice extent as recorded by satellites has declined by about 3% per decade (Serreze and Francis 2006). Although essentially all global climate models predict this Arctic sensitivity (Serreze and Francis 2006) and despite the recent activity in

Arctic studies, the reason behind this climate sensitivity has not been explained. This clearly demonstrates a

lack in understanding of the Arctic region, which can likely be attributed to its remoteness and lack of observations, especially during Arctic winter when it is draped in darkness. This region is extremely complex and unique compared with other regions of the world (Curry et al. 1996).

1.1 Space-based Remote Sensing

The Arctic wintertime clouds and precipitation are poorly understood (within the scientific community), which can be attributed mainly due to its remoteness and lack of ground-based observations. In addition, the use of visible and infrared satellites for Arctic winter cloud observations have been nearly impossible due to the lack of sunlight and negligible differences between surface and cloud temperatures, respectively. Also, because many cloud layers over the Arctic and upper troposphere are subvisible, they have long been overlooked or undetected by standard observations (Curry et al. 1996). Given the difficulty in Arctic wintertime cloud observations, numerous studies have attempted cloud climatologies (Husche 1969, Vowinckel 1962, Gorshkov 1983, Beryland and Strokina 1980, Warren et al. 1988, Hahn et al. 1995, and Intrieri et al. 2001). These climatologies show broad agreement, with a minimum total cloud cover during the winter of 40%-68% (Curry et al. 1996). With the recent launch of two successful satellites, CloudSat (microwave cloud profiling radar) and CALIPSO (Cloud-Aerosol Lidar and Infrared Pathfinder Satellite Observations), into the A-train constellation of space-borne atmospheric observatories, Arctic cloud observations have become much more ubiquitous. In addition to these relatively new observations, the polar orbiting nature of the A-train satellites provides a temporal resolution of the Arctic region that is maximized relative to the rest of the world. This becomes highly valuable when attempting to observe the evolution and lifecycle of atmospheric events.

1.2 Thin Ice Clouds

Clouds play an important role in the Arctic Climate (Prenni et al. 2007). Over numerous decades the influence of aerosols on cloud microphysics has been studied and of most importance are two leading studies which suggest that aerosols affect cloud albedo: Twomey (1977) and Albrecht (1989). By increasing droplet concentration and thereby the optical thickness of a cloud, pollution acts to increase the albedo of warm clouds (Twomey 1977), thereby reducing the incoming solar radiation and cooling the earth's surface. In addition, the increase in aerosol concentrations over the oceans may increase the amount of low-level cloudiness associated with a decrease in droplet size would contribute to a retarding of drizzle formation and thus act to cool the surface (Albrecht 1989).

There have been numerous studies in the effects of aerosols on Arctic summer and transitional season cloud microphysics. Using an eddy-resolving model Harrington et al. (1999) simulated Arctic summertime stratus and found that the production of drizzle-sized drops is strongly dependent upon parcel cloud-top residence time for both radiative- and nonradiative-influenced growth. While for mixed-phase clouds, Harrington et al. (1999) used a cloud resolving model version of the Regional Atmospheric Modeling System (RAMS) to show a new mechanism of multiple-layer cloud formation in the Arctic. In addition, using a multi-month cloud resolving model version of RAMS, Carrio et al. (2005) showed that IN entrainment of polluted air overriding the Arctic inversion may have a significant impact on sea-ice freezing/melting rates when mixed phased clouds are present. Aside from summer and transitional season clouds, fewer studies of Arctic winter cloud microphysics have been conducted. Girard and Blanchet (2001) describe a microphysical parameterization for low-levels clouds that are characteristic of Arctic winter. Using the parameterization, they find that diamond dust events are a significant contributor to the surface longwave radiation flux. In addition to modeling studies, there have been numerous Arctic observational studies. Curry et al. (1996) gives an overview of Arctic cloud and radiation characteristics, while Adams et al. (2000) and Overland et al. (1997) describe the regional variability of the Arctic fall and winter heat budget and winter temperatures, respectively. Lubin and Vogelmann (2005) uses multisensor radiometric data to show that enhanced aerosol concentrations alter the microphysical properties of Arctic clouds which leads to an increase of 3.4 Watts/m^2 in the surface longwave fluxes.

While there have been numerous studies in the effects of aerosols on summer, transitional, and wintertime boundary layer cloud microphysics, few have been directed toward the effects of anthropogenic aerosols on mid to upper level cold cloud microphysics. This is primarily due to the remoteness and difficulty in obtaining observations for these regions. Despite the difficulties in studying the Arctic mid-level atmosphere, it offers many advantages for investigating the interaction between clouds and aerosols when compared to the mid-latitudes. First, the Arctic wintertime atmosphere is cold and stable, which acts to dramatically reduce the vertical motion and therefore eliminate sources of error in the formation of clouds. In addition, the absence of solar radiation also eliminates a source of error in the radiative energy balance. Finally, the remoteness relative to the industrial world provides a clean background atmosphere that can allow for anthropogenic aerosols to be more distinguishable.

As described in the previous sub-section, the recent launch of both CloudSat and CALIPSO have provided unique and valuable data regarding the nocturnal Arctic wintertime atmosphere. The combination of CloudSat's cloud profiling radar and CALIPSO's cloud-aerosol lidar provides insight into how water and aerosol interact in the Arctic atmosphere, and can be an indirect way of assessing ice crystal growth rate. Because radar reflectivity varies with the sixth power of particle diameter while lidar backscatter is a function of only the second power of particle diameter, there is a much stronger dependence on particle size for radar reflectivity. Typically, ice crystals smaller than about 20μm in size cannot be detected by the CloudSat radar, but are visible to the CALIPSO lidar. This window of particle size dependence between the two instruments offers a great tool in indirectly assessing the type of ice crystal population observed. If the lidar receives a large backscatter from assumed ice crystals that are subvisible to the radar, then it can be assumed that there are large numbers of relatively small ice crystals. In contrast, for the same given lidar backscatter from ice crystals that are seen by the radar, then it can be assumed that there are lower numbers of relatively large ice crystals. Based on these assumptions, it can be said that the depth of the transition zone between the clear air above cloud top visible to the lidar and the region below cloud top that first is detectable by the radar is directly related to ice crystal growth rate. A very thin transition region would indicate a high ice crystal growth rate, and vice versa. It is hypothesized that concentrations of ice nuclei (IN) affect the depth of the transition zone, and thus directly affect the ice crystal growth rate. With lower IN concentrations, there would be less activated ice crystals that would reduce the competition for available water vapor. This lack of competition would allow the low concentration of activated ice crystals to grow relatively large and fast, therefore decreasing the depth of the transition zone. Conversely, with higher IN concentrations, the number of activated ice crystals would be large and the competition for available water vapor amongst them would increase. This higher competition would make it more difficult for the ice crystals to grow large, and therefore the ice crystal growth rate would be lower and the transition zone would be deeper. Essentially the two scenarios, high and low IN concentrations, have comparable amounts of mass, however they are distributed in a smaller number of large particles for the low IN concentration case, and a larger number of small particles for the high IN concentration case.

In January of 2007, observations using CloudSat and CALIPSO have been made of these optically Thin Ice Clouds (TIC) described above (Grenier et al. 2009). TIC's are observed above the Arctic inversion and generally extend up to 6km AGL. They can be classified into two categories: 1) TIC-1, which is detectable by lidar only, and 2) TIC-2, which is detectable by both lidar and radar. According to Grenier et al. 2009, TIC-2's are often surrounded with air characterized by enhanced lidar backscatter ratios that correspond to aerosol concentrations significantly above the background level, based on a depolarization ratio technique. It is well known that these high levels of mid-tropospheric aerosols are transported over long distances to the Arctic during the cold season from industrial regions in Europe, Russia and Southeastern Asia (Christensen 1997). According to Grenier et al. (2009), during winter and spring in the Arctic, 30% to 50% of the aerosol mass composition is typically sulfuric acid. Direct observations (Bigg 1980) show that about 80 % of the insoluble particles are coated with a sulfuric acid layer that forms in a high humidity environment preventing freezing at sufficient concentrations and reducing the IN concentrations by 1 to 3 orders of magnitudes (Borys 1989). Blanchet and Girard (2001) show that when air-cooling is slow and vapor pressure is in near equilibrium with aerosol surfaces, either homogeneous or heterogeneous nucleation selectively favors the ice nucleation at the large end of the particle size spectrum. Therefore, with a low number of large IN within a high humidity environment, ice embryos should therefore grow explosively towards precipitation sized crystals.

This study focuses on the microphysical mechanisms that generate a TIC-2 formation due to acidic coating of IN particles. While Grenier et al. (2009) is an observational study that provides data regarding the occurrence of the TIC's, this study uses modeling [RAMS] to understand the formation mechanisms of these TIC's. First, a TIC-2 event that occurred over the Polar Environment Atmospheric Research Laboratory (PEARL) on 7 January 2007 is used as a case study to understand the microphysics and validate the model versus observations. CloudSat and CALIPSO are solely used to illustrate the identification technique employed by Grenier et al. (2009) for this TIC-2 event. Based on the PEARL case study, a sensitivity experiment is created that varies the initial conditions in order to understand which environmental conditions maximize the production of a TIC-2 event.

For this study, radiosonde profiles taken from PEARL during the TIC-2 event are used as in-situ observations to simulate this atmospheric phenomenon. By varying IN concentrations, RAMS will simulate the difference between TIC-1 and TIC-2 cases (i.e. the sulfuric acid coating of IN particles). TIC-2 cases will be simulated with very low IN concentrations, whereas TIC-1 cases will be simulated under high IN concentrations. In the TIC-2 cases where IN concentrations are low, the ice crystals are hypothesized to have the ability to grow large enough to readily precipitate out. These precipitation-sized ice crystals would then act to remove moisture from the Arctic atmosphere. Because water vapor is the dominant greenhouse gas in the atmosphere, it is important to obtain a better understanding of the microphysical processes that act to potentially dehydrate the Arctic wintertime atmosphere.

1.3 Goals of this Study

The goal is this study is to simulate Arctic wintertime thin ice clouds using the current Colorado State University RAMS 4.3.0 atmospheric model. Initially, model results will be compared directly to radar observations to ensure the success of the simulations. Based on successful simulations, sensitivity testing will ensue and by simulating these Arctic clouds we hope to gain a better understanding of the following questions:

(1) Do different IN concentrations change the structure of the clouds microphysically? By initializing the model with low ice nuclei concentrations, RAMS will be simulating the effect of IN particles being rendered inactive

due to coating of sulfate aerosols. Conversely, simulations with high ice nuclei concentrations mimic the cases in which aerosol coating does not occur. We hope to observe different crystal growth rates and a significant change in effective diameter in ice crystal species.

(2) What environmental conditions are necessary to maximize the difference in ice crystal growth rate between the high IN and low IN concentration scenarios? We use a case study as a benchmark to further understand and find the environmental conditions where the ice crystal growth rate is maximized. By independently varying the observed temperature profile versus the observed moisture profile, we will observe how the cloud microphysics change based on temperature alone, supersaturation alone, and both temperature and supersaturation.

(3) Are both homogeneous and heterogeneous nucleation of ice operational in the clouds? During the sensitivity testing, we hope to identify the main nucleation process responsible for the formation and persistence of the thin ice clouds. CCN and haze particle concentrations along with IN concentrations will be varied to answer this question.

The remainder of this paper is organized into three chapters, each highlighting important aspects of this study. An effort has been made to compartmentalize each chapter, such that each stands on its own to some extent, with references to other sections and papers should further detail be desired. A conclusion summarizes the model results during the study and includes a number of recommendations for future studies.

CHAPTER 2

THE MODEL

This chapter provides an introduction to the RAMS model currently in use at Colorado State University in addition to a more detailed description of the model's microphysics scheme. First, a brief overview of the model's evolution, development and current usage is provided. Next, the microphysics scheme used in this experiment is explained in great detail, as it is the focus of this thesis. After that, a brief summary of the current radiation scheme is described. Finally, the nudging scheme utilized to help the model stay on track with observations is discussed.

By an integration of three related models in the early 1980's, the RAMS concept was invented at Colorado State University. These three models are described in a paper by Pielke et al. (1992). The three models are the CSU cloud/mesoscale mode by Tripoli and Cotton (1982), a hydrostatic version of the cloud model by Tremback (1990), and the sea breeze model by Mahrer and Pielke (1977). After years of development, the first version to be widely distributed, version 2c, was released in 1991. This version is the backbone for all of the RAMS models in use today, however there have been many modifications since its debut. RAMS can be adapted to a specific use. For instance, RAMS can be configured to simulate global circulations all the way down to boundary layer eddies. Cotton et al. (2001) provides examples of some applications of the model.

For this experiment, the main configuration of RAMS is as a large eddy simulation (LES) in order to fully resolve the microphysics coupled to cloud-scale motions.

The most recent version in use at CSU (the version used in this experiment) is RAMS 4.3.0 and it is a non-hydrostatic model, using a rotated polar-stereographic horizontal grid, and a staggered Arakawa-C vertical grid. Time differencing is done via a hybrid combination of the leapfrog scheme, used for the calculation of the Exner function, and a forward-in-time scheme, used for all other variables. Turbulence closure is calculated from one of four methods: 1) Mellor-Yamada level 2.5 scheme, using an ensemble-averaged total kinetic energy (TKE) (Mellor and Yamada 1982), 2) Anisotropic deformation, 3) Isotropic deformation, and 4) Deardorff level 2.5 scheme, which calculates eddy viscosity as a function of TKE. For this experiment, option four was employed. The most recent radiation scheme is Harrington (1997) longwave/shortwave model; it uses a two-stream scheme that interacts with liquid and ice hydrometeor size-spectra. Convective parameterization is done either with the Kuo or Kain-Fritsch methods, with explicit cloud representations for smaller grids, however due to the small vertical velocities observed during Arctic winter this option was turned off. At the lower boundary, a soil/vegetation/snow model [LEAF2, Walko et al. (2000)] is used over land with vegetation type set to ice cap/glacier, while the lateral boundaries are set to be cyclic. See Table 2.1 for a summary of RAMS model physics and boundary schemes used throughout this study.

Table 2.1: Chart of model physics options used throughout experiment.

Model Aspect	Setting
Microphysics	Two-moment bulk microphysics – Saleeby and Cotton (2008) Includes cloud water, rain, pristine ice, snow, aggregates, graupel, hail
Turbulence scheme	Deardorff level 2.5 scheme – calculates eddy viscosity as a function of TKE
Radiation scheme	Two-stream parameterization developed by Harrington (1997)
Lateral boundary	Cyclic
Surface boundary	LEAF-2 scheme - Walko et al. (2000) set to ice cap/glacier
Top boundary	Rigid lid with a Rayleigh friction layer

2.1 Microphysics

Water is categorized in eight forms: vapor, cloud droplets, rain, pristine ice, snow aggregates, graupel and hail. Both cloud droplets and rain are liquid water, however they may be supercooled. Pristine ice, snow, and aggregates are all assumed to be completely frozen, while both graupel and hail are mixed-phase categories (Walko et al. 1995). Pristine ice is grown purely by vapor deposition. Once a pristine ice crystal reaches a user specified threshold (usually ~120μm), then it transfers over to the snow category and then can further grow by both vapor deposition and riming.

Within each category, the hydrometeors are assumed to conform to a generalized gamma distribution described by Flatau et al. (1989) and Verlinde et al. (1990), given by

$$n(D)=\frac{N_t}{\Gamma(\nu)}\left(\frac{D}{D_n}\right)^{\nu-1}\frac{1}{D_n}\exp\left(-\frac{D}{D_n}\right) \quad (2.1)$$

where $n(D)$ is the number of particles of diameter D, N_t is the total number of particles, ν is the shape parameter that controls the relative amount of smaller vs. larger hydrometeors, and D_n is some characteristic diameter of the distribution. The characteristic diameter, D_n, serves as a diameter scaling factor for the distribution and acts to nondimensionalize D (Walko et al. 1995). Any moment, P, of the above distribution is given by

$$\int_0^\infty D^P\, n(D)dD = D_n^P\,\frac{\Gamma(\nu+P)}{\Gamma(\nu)}. \quad (2.2)$$

In order to utilize the above equation to provide a solution to the integral, the property of the hydrometeor species must be expressed as a power of D. Two such properties, mass m and terminal velocity v_t, are expressed as power law formulas

$$m=\alpha_m D^{\beta_m} \quad (2.3)$$

$$v_t=\alpha_{v_t} D^{\beta_{v_t}} \quad (2.4)$$

By taking (2.3) [the mass equation], converting it to a concentration-normalized integral, multiplying by N_t, and dividing by air density ρ_a, the mass mixing ratio for a given hydrometeor category can be shown as

$$r = \frac{N_t}{\rho_a} \alpha_m D_n^{\beta_m} \frac{\Gamma(\nu + \beta_m)}{\Gamma(\nu)} \tag{2.5}$$

where α_m, β_m, α_{vt}, and β_{vt} are four parameters specified by a look-up table stored in RAMS, generally based on the type of simulation, and ν is determined either from observations, trial and error, or sensitivity experiments. All parameters are held fixed in time and space for the duration of the simulation, however the pristine ice and snow categories can be switched during a simulation based on a pre-determined algorithm (Harrington et al. 1995).

Cloud droplet number is predicted from a specified constant of cloud condensation nuclei (CCN). The number of CCN that activate are a function of air temperature, Lagrangian supersaturation production rate and number concentration of CCN. Other factors such as CCN chemistry, mean radius, and spectral width are considered fixed for the simulation. Based on the mentioned CCN characteristics and environmental factors, RAMS accesses a lookup table that was previously generated from a detailed bin-parcel model to determine the fraction of CCN that nucleate into cloud droplets (Saleeby and Cotton 2008).

Nucleation of pristine ice crystals may be divided into two general categories: heterogeneous nucleation and homogeneous nucleation. Heterogeneous nucleation occurs when an ice nucleus (IN) initiates the formation of an ice crystal from vapor or liquid, while homogeneous nucleation occurs without the presence of an IN. A brief description of these types of nucleation is described below.

Heterogeneous nucleation can further be broken down into different forms. First, depositional nucleation occurs when vapor molecules attach to an IN. In RAMS, this may occur any time the ambient vapor mixing ratio exceeds saturation over ice and the temperature is below -5°C. Next, condensation-freezing nucleation occurs when an intermittently mixed aerosol has characteristics of both an IN and a CCN. The ice crystal forms from vapor molecules attaching to the aerosol as liquid, due to the CCN property, and then freezing from its IN property. In RAMS, this form of heterogeneous nucleation may occur when supersaturation with respect to both ice and liquid is present and the temperature is below -2°C. Both of these types of nucleation are represented by a single formula (Meyers et al. 1992) from published continuous flow diffusion chamber data sets. However, Cotton et al. (2003) recognized the necessity of vertical and horizontal variations in IN concentrations and modified the equation to include the prognostic variable N_{IN} (Levin and Cotton 2009) as shown by:

$$N_{id} = N_{IN} \exp\left[12.96(Si-1)\right], \tag{2.6}$$

where N_{id} (l^{-1}) is the number of pristine ice crystals predicted due to deposition-condensation freezing, N_{IN} (l^{-1}) is the IN concentration, and S_i is the supersaturation ratio with respect to ice. N_{id} represents the total number of crystals allowed to nucleate under the given environmental conditions, and is not dependent on time or the length of the model timestep. If N_{id} is greater than the number of pristine ice crystals, then the remaining amount is allowed to nucleate into crystals. However, if N_{id} is less than the number of pristine ice crystals, then the current ice crystals are left alone. Lastly, contact freezing occurs when an IN comes into contact with an existing supercooled cloud water droplet through the processes of diffusiophoresis, thermophoresis, and Brownian motion, and is represented by the equation

$$N_{ic} = \exp\left[a + b(273.15 - T_c)\right], \tag{2.7}$$

where N_{ic} is the number of ice crystals formed by contact nucleation (l^{-1}), a = -2.80 and b = 0.262. The contact nucleation process is secondary to the ice production by deposition/condensation-freezing.

At colder temperatures, such as during Arctic winter, homogeneous nucleation of water into ice crystals becomes more important. Homogeneous nucleation of supercooled water droplets is a process whereby a liquid water drop spontaneously freezes into an ice crystal without the aid of an IN. It is strongly dependent on three characteristics: 1) drop size, where larger drops are more likely to freeze, 2) temperature, where RAMS applies the nucleation formula when temperatures are less that -35°C, and 3) the impurities within the water, which is taken into account within the haze nucleation scheme. DeMott et al. (1994) describe in detail the process of homogeneous freezing of CCN solution drops (i.e. homogeneous haze nucleation). However in short, solution drops freeze at warmer temperatures than for pure water drops and below water saturation where freezing can occur on solution drops or haze particles. These characteristics of solution drops and haze particles are due to non-ideal ionic interactions combined with the effect of curvature and equilibrium solution effects.

2.2 Radiation

A two-stream radiative transfer model (Harrington et al. 1999) is used for this study. The two-stream model solves the radiative transfer equations for three gaseous constituents, H_2O, O_3, and CO_2 and the optical effects of the hydrometeor size spectra. Gaseous absorption is calculated by following the fast exponential sum fitting of transmissions method proposed by Ritter and Geleyn (1992). Lorenz-Mie theory is used to compute the optical properties for water drops, while the theory of Mitchell et al. (1996) is used for non-spherical ice crystals. For each hydrometeor species, the band-averaged values of optical properties are computed for the assumed gamma distribution basis function following the method of Slingo and Schrecker (1982).

The radiation model works closely with the bin microphysical model by using a method of computing the optical properties whereby bin averages of the appropriate quantities are computed beforehand, and then summed with appropriate weights during the simulation (Harrington et al. 1997). This method allows simulation of changes in radiative heating as droplet spectra broaden to precipitation sizes and even feedbacks of radiation on droplet and ice particle vapor deposition growth (Cotton et al. 2001; Harrington et al. 1999; Wu et al. 2000).

2.3 Nudging Scheme

This study utilizes RAMS as a cloud-resolving model (CRM). In doing so, it is pertinent to assume the model grid is significantly smaller than the synoptic scale cloud being simulated; therefore the use of cyclical boundary conditions is implemented. Because of this assumption, we cannot take large-scale observations into account and therefore the large-scale tendencies are used.

This section describes how large-scale tendencies are implemented into this experiment during simulations. To apply large-scale tendencies to the model, radiosonde profiles taken every 12 hours are strategically ingested into the model. By using large-scale tendencies during simulations, it provides two benefits: 1) observations provide information about the large scale forcing that the microscale model cannot obtain using cyclic boundaries, and 2) observations help keep the model from diverging too far from reality. These large-scale tendencies have been utilized in the model two different ways – linear large-scale tendencies and large-scale tendencies as nudging – and is further described below.

Linear large-scale tendencies is a shorthand method to applying observations to the model. These linear tendencies interpolate the observation profile while in between observation times and apply it to the current model timestep (Carrio et al. 2005). It can be shown by equation below

$$\psi(k,i,t) = \psi(k,i,t-\Delta t) + \mathrm{mod}\,el + \alpha\left(\frac{\psi_{obs}(k,t-\Delta t)}{\Delta t}\cdot\tau\right), \tag{2.8}$$

where $\psi(k,i,t)$ is the predicted value of a linear tendency variable at the end of the current timestep; $\psi(k,i,t-\Delta t)$ is the model value at the end of the previous time step; the model includes advection, diffusion, thermodynamic effects, etc.; α is the linear intensity ranging from zero to one, ψ_{obs}(k,t) is the vertical profile being nudged to and is a function of the vertical index k; Δt is the time difference between observations (s^{-1}), and T is the model timestep. As α approaches zero(one), the model becomes less(more) influenced by the observations.

A more detailed and effective method to applying observations to the model is using the large-scale tendencies as nudging. Nudging, a Newtonian relaxation technique, takes the difference between a linearly interpolated profile of observations and a horizontally-averaged model profile and then adds the anomalies from the horizontally averaged model profile back. This method of is a more precise application of tendencies in that the small-scale features and perturbations are preserved for each timestep (Carrio et al. 2005). It can be shown by the equation below

$$\psi(k,i,t) = \psi(k,i,t-\Delta t) + \mathrm{mod}el + \alpha\left(\psi_{obs}(k,t-\Delta t) - \psi H(k,t-\Delta t)/\tau\right), \tag{2.9}$$

where $\psi(k,i,t)$ is the predicted value of a nudged variable at the end of the current timestep; $\psi(k,i,t-\Delta t)$ is the model value at the end of the previous time step; the model includes advection, diffusion, thermodynamic effects, etc.; α is the nudging intensity ranging from zero to one, ψ_{obs}(k,t) is the vertical profile being nudged to and is a function of the vertical index k; $\psi H(k,t-\Delta t)$ is the horizontal average at the end of the previous time step, and τ denotes the time scale. As α approaches zero(one), the model becomes less(more) influenced by the observations.

The following two chapters will describe the specific RAMS setup and usage for each experiment. Chapter 3 utilizes RAMS for a case study, while Chapter 4 explains the model setup for a sensitivity experiment.

CHAPTER 3

PEARL THIN ICE CLOUD CASE STUDY (PTIC)

This case is one of several investigated by Grenier at al. (2009). It has been chosen as the case study in this experiment for two reasons: 1) it theoretically represents a classic example of TIC-2, and 2) it occurred over a region in which ample ground-based observations are available – a characteristic not common within the Arctic. This case study, herein named PTIC (PEARL Thin Ice Cloud), is a two-day event that occurred over the Northern Arctic from 7-8 of January 2007. To allow for model spinup, which is the time it takes for the model to develop a consistent distribution of eddies, an additional twelve hours were used. Therefore, two and a half days of data from 12Z on 6 January through 00Z 9 January were used for simulations. This chapter will describe in detail the meteorological background of this case, the model setup and methods used for simulations, the results of the simulations, and analysis of the results.

3.1 Meteorology

This case study occurred over a remote Canadian operated research facility, Polar Environment Atmospheric Research Laboratory (PEARL), in Eureka, Nunavut, Canada. It is located on Ellesmere Island at approximately 80°N and 86°W. PEARL is equipped with an operational weather station that continually records meteorological data, launches twice daily radiosondes, and has an array of atmospheric instruments. For this experiment, ground–based zenith pointing radar data, shown in Figure 3.1, were used as means of model validation data. It provides a time vs. height illustration of reflectivity at the site. The observations used to nudge RAMS were taken from seven radiosonde profiles, each separated by twelve hours from 12Z 6 January through 00Z 9 January 2007 (data obtained from http://raob.fsl.noaa.gov/).

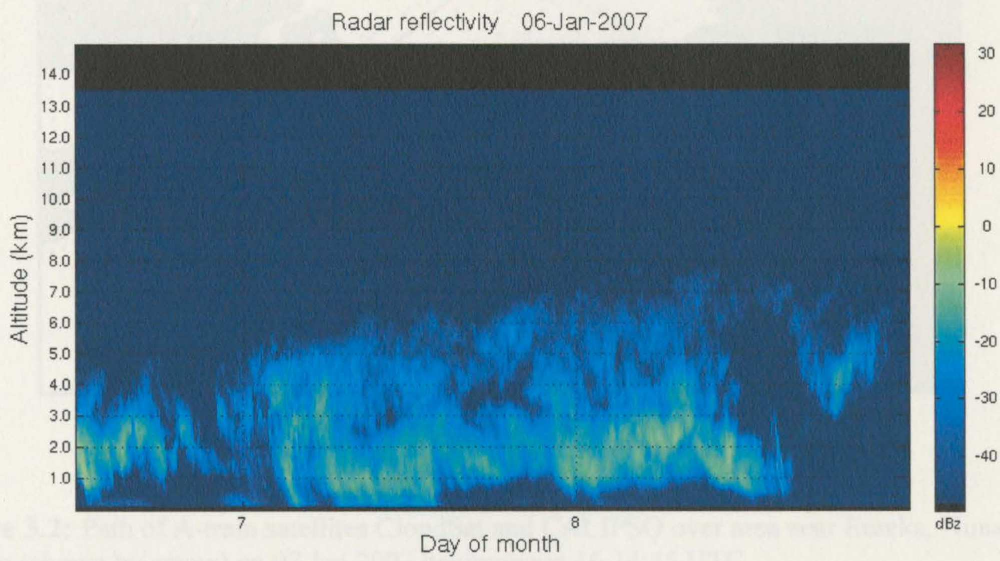

Figure 3.1: Vertical profile of radar reflectivity above PEARL in Eureka, Canada as a function of time. Time of measurements extend from 12Z 6 Jan through 00Z 9 Jan 2007. PTIC focuses on 7-8 Jan.
(Source: http://lidar.ssec.wisc.edu/cgi-bin/processeddata/retrievedata.cgi)

During PTIC, two satellites from the A-Train constellation of space-borne atmospheric instruments, CloudSat and CALIPSO, passed almost directly over PEARL, as shown by Figure 3.2. Figure 3.3 shows data captured from CloudSat's Cloud Profiling Radar (CPR) of the PTIC event (outlined by the rectangle), while Figure 3.4 is of the same region captured from CALIPSO. Reflectivity values for PTIC range from approximately -30 dBZe to near 0 dBZe. Further to the northwest, bounded by latitudes 73°N and 69°N (shown by oval), similar reflectivity values are observed. By comparing these two regions, the PTIC event can be shown to be to be of TIC-2 nature.

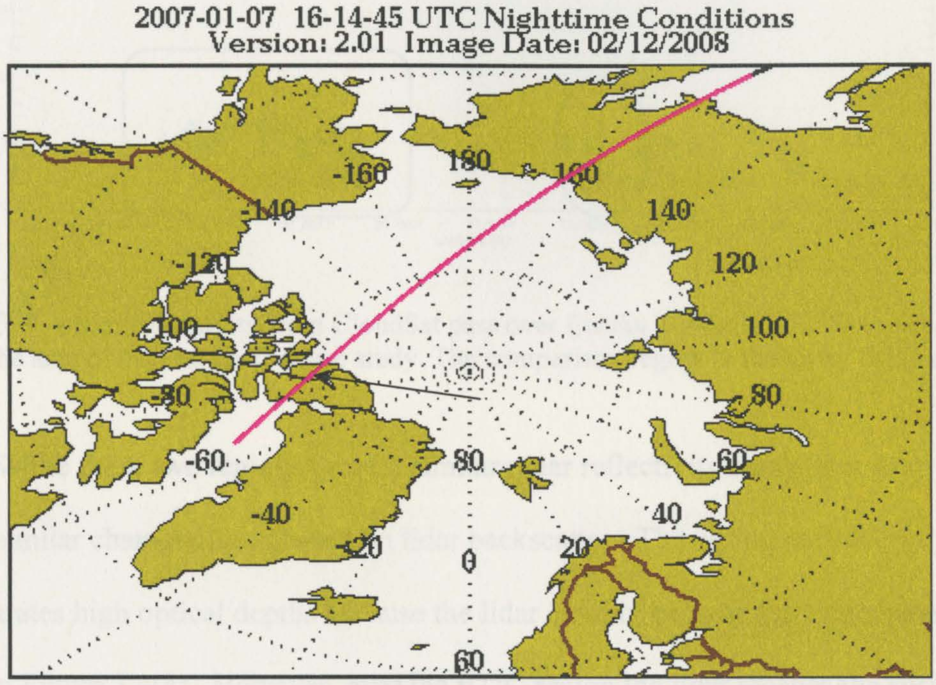

Figure 3.2: Path of A-train satellites CloudSat and CALIPSO over area near Eureka, Nunavut, Canada (shown by arrow) on 07 Jan 2007 beginning at 16:14:45 UTC.
(Source: http://www-calipso.larc.nasa.gov/)

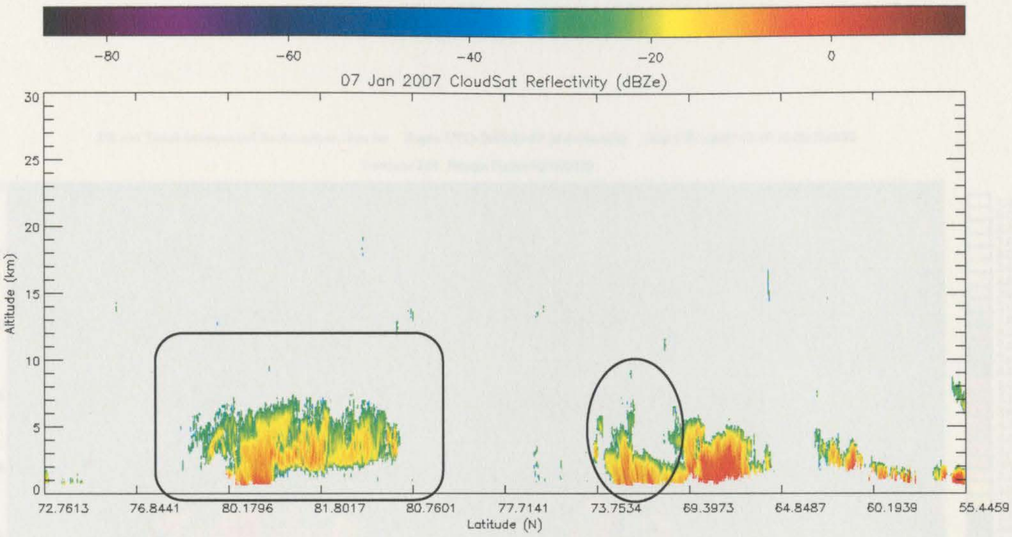

Figure 3.3: Radar reflectivity from CloudSat pass over Eureka during PTIC. The rectangle depicts the area of interest for the case study. The comparison region is shown by the oval.

While these two regions present similar radar reflectivity signatures, they do not exhibit similar characteristics based on lidar backscatter. The region northwest of PTIC demonstrates high optical depths because the lidar quickly became fully attenuated, as shown in Figure 3.4(a). However, over the PTIC region the lidar reaches the surface and displays much lower attenuated backscatter. Because radar reflectivity is a function of the sixth power of particle diameter, while lidar backscatter is proportional to the cross-sectional area of the particle, and therefore the square of the diameter, these signatures indicate that the PTIC region is comprised of a small number of large particles. In addition, Figure 3.4(b) indicates that the atmosphere contains aerosols, which would likely be sulfuric in nature that coat IN and is hypothesized to render them ineffective. With an atmosphere of coated IN particles and signatures of a cloud comprised of a small number of large particles, this case can be said to be of TIC-2 nature.

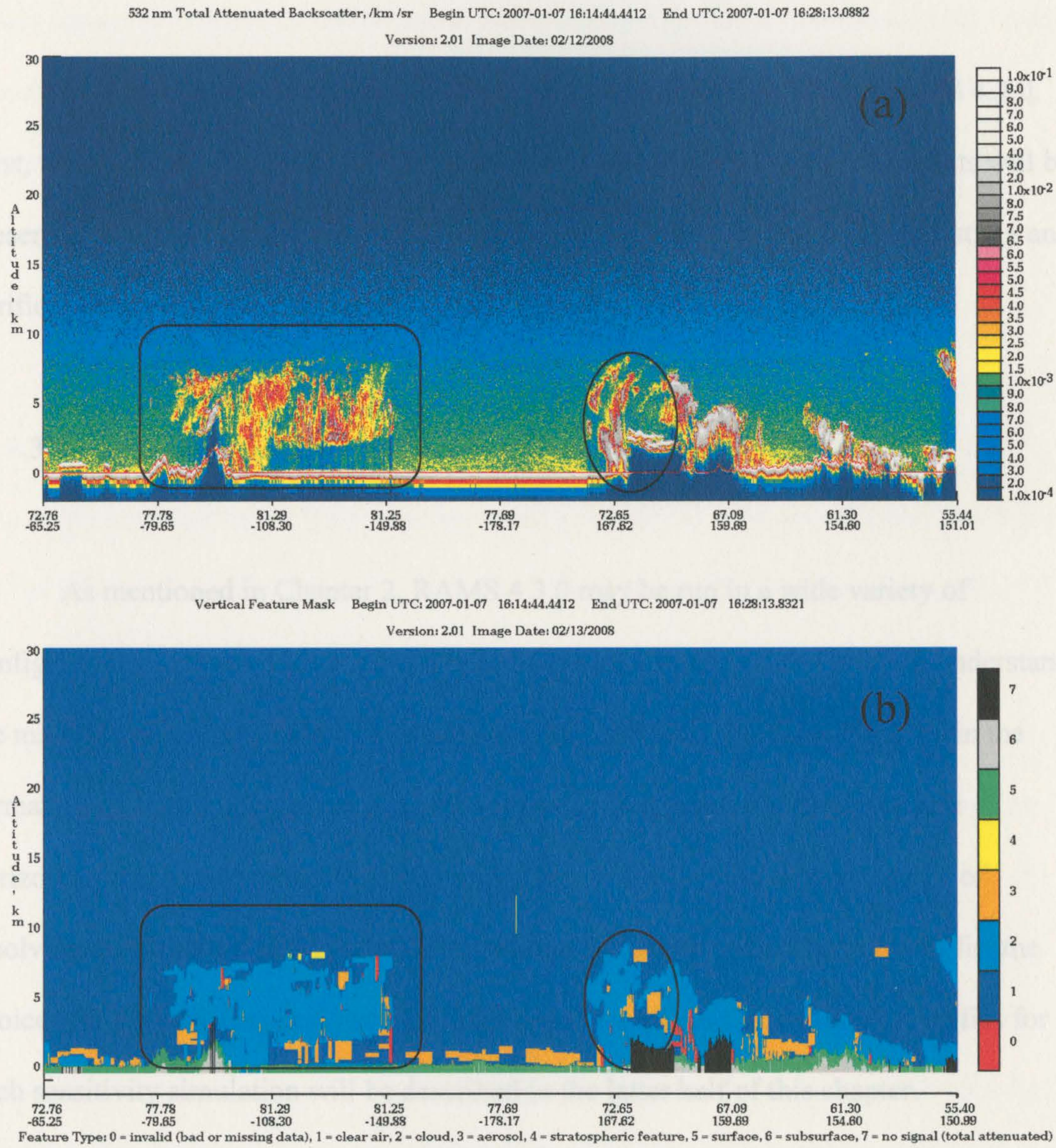

Figure 3.4: (a) 532 nm total attenuated lidar backscatter from CALIPSO pass over Eureka during PTIC. The rectangle depicts the area of interest for the case study and the comparison region is shown by the oval. It is of note that the PTIC region did not show signs of full attenuation while the region of comparison did. (b) Vertical feature mask of same swath as (a). The low tropospheric aerosols can be seen beneath the cloud and shaded orange. (Source: http://www-calipso.larc.nasa.gov/)

3.2 Model Setup and Testing

This section provides the methodology of simulating PTIC using RAMS 4.3.0. First, the model configuration will be described. Then a series of sensitivity tests will be presented that function as both a basis of understanding the science of the case study and verifications against observations.

3.2.1 Model Setup

As mentioned in Chapter 2, RAMS 4.3.0 may be run in a wide variety of configurations. However, it is crucial to simulate on a small scale in order to understand the microphysics and cloud-scale dynamics of the complex processes involved in the formation of TIC-2. Therefore, RAMS was configured as a CRM model whose horizontal- and time-averages can be viewed as a single column model capable of resolving the turbulent eddies containing most of the energy. This section will list the choices for the variables that were left unchanged for all case study runs. Specifics for each sensitivity simulation will be described in the latter half of this chapter.

As described in Section 2.3, radiosonde observations of vertical profiles taken from Eureka, Canada were used to nudge the model and act as large scale forcing. This is extremely efficient with computational power because it is not necessary to utilize the nested grid option within RAMS. Additionally, because we are simulating the microphysics of a synoptic-scale event, the entire model can be treated as an internal column within the cloud. With this characteristic it is not necessary to configure RAMS to a three-dimensional model, as both horizontal dimensions should theoretically be nearly identical. Although turbulence is treated differently for three-dimensional versus two-dimensional simulations, the arctic winter free atmosphere generally does not produce significant turbulence. This is because during Arctic winter nearly all of the energy originates from the surface, which is locked up in the boundary layer by the strong inversion.

To verify lack of turbulence, a brief look at the dynamics of PTIC was necessary. First, the horizontal average of total kinetic energy (TKE) was calculated for PTIC. Above the boundary layer, TKE was too small to break the minimum threshold of 5.0 x 10^{-4} m^2s^{-2}. As a result of the small TKE values, additional data was desired and the horizontal variance of vertical velocity (w') in ms^{-1} was calculated, which showed values on the order of 10^{-4} and smaller for the entire simulation. These very small values of TKE and w' demonstrate the lack of free atmosphere turbulence for PTIC. To further verify the two-dimensional assumption used in this experiment, Figures 3.5 (a) and (b) show the total ice mixing ratios for both the two-dimensional and three-dimensional simulations of PTIC. It is evident that negligible differences existed between the simulations and is confirmed in Figure 3.5 (c) showing less than 1% error between the two simulations. As a result of these data, the framework of RAMS was set to a single, two-dimensional grid.

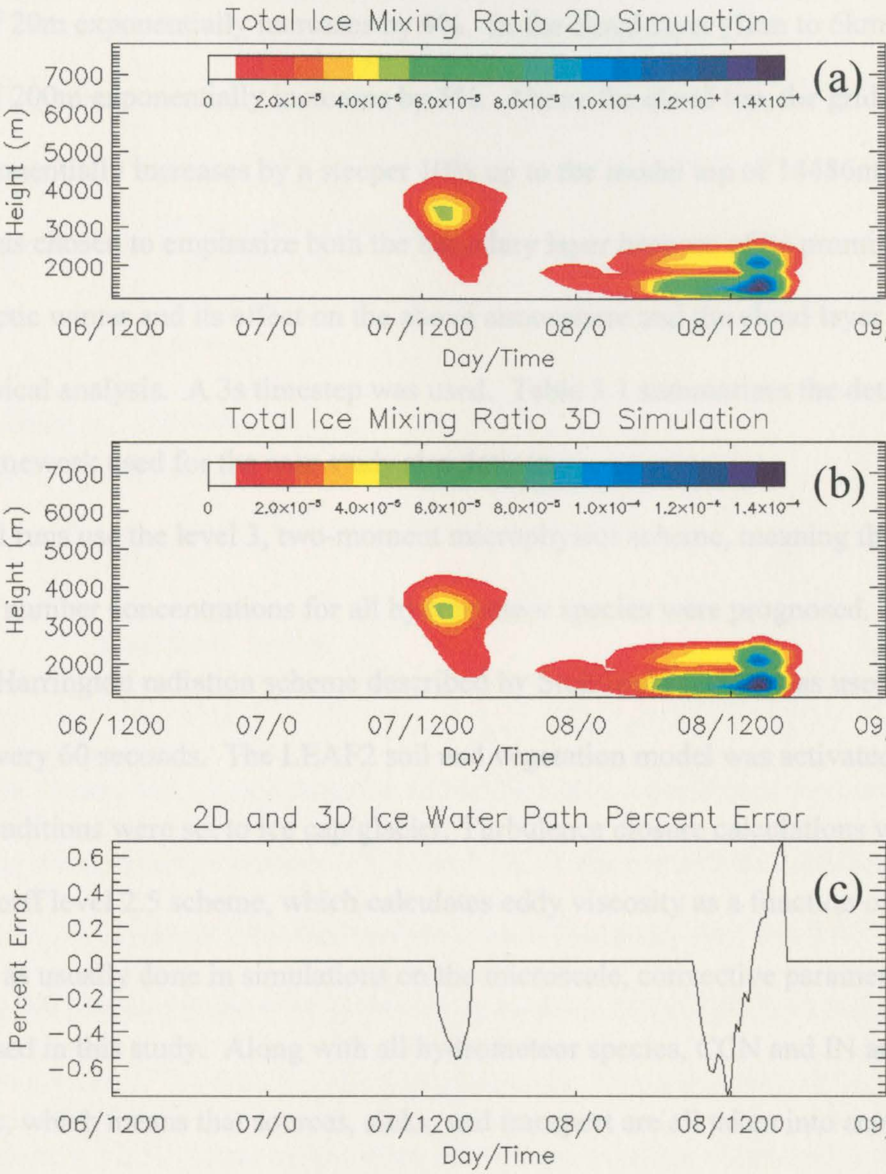

Figure 3.5: Total ice mixing ratios (g/kg) of PTIC with high IN concentrations for: (a) two-dimensional simulation, and (b) three-dimensional simulation. (c) Ice water path percent error between (a) and (b).

To adequately resolve all relevant microphysical processes, the horizontal grid spacing was set to 100m and the domain was 10km long. For the vertical resolution, 47 vertical levels broken into three categories of boundary layer, cloud layer, and above cloud top were used for all simulations. For the boundary layer (surface to 1km), the grid spacing of 20m exponentially increases by 9%. In the cloud layer (1km to 6km), the grid spacing of 200m exponentially increases by 5%. Above the cloud top, the grid spacing of 200m exponentially increases by a steeper 10% up to the model top of 14486m. This spacing was chosen to emphasize both the boundary layer because of its prominence during Arctic winter and its effect on the above atmosphere and the cloud layer for the microphysical analysis. A 3s timestep was used. Table 3.1 summarizes the details in the model framework used for the case study simulations.

All runs use the level 3, two-moment microphysics scheme, meaning that mixing ratios and number concentrations for all hydrometeor species were prognosed. The modified Harrington radiation scheme described by Stokowski (2005) was used and updated every 60 seconds. The LEAF2 soil and vegetation model was activated and the surface conditions were set to ice cap/glacier. Turbulence closure calculations were set to the Deardorff level 2.5 scheme, which calculates eddy viscosity as a function of TKE. However, as usually done in simulations on the microscale, convective parameterization was not used in this study. Along with all hydrometeor species, CCN and IN are fully prognostic, which means that sources, sinks, and transport are all taken into account. For model initialization CCN and IN concentrations were varied based on the type of sensitivity testing and will be described in the following section.

Table 3.1: Chart of framework settings used in all PTIC simulations.

Framework Aspect	Setting
Model configuration	Two-dimensional, single grid cloud resolving model
Horizontal grid	100 m grid spacing 100 horizontal grid points
Vertical grid	47 vertical levels Variable grid spacing with emphasis on boundary layer and cloud layer
Timestep	3 seconds
Simulation length	60 hours

3.2.2 Sensitivity Testing

This section will list and describe all the simulations performed on this case study. To simulate the differences between TIC-1 and TIC-2, the concentrations of ice nuclei (shown by N_{IN} in Equation 2.6) were varied for each sensitivity run. For TIC-1 simulation, IN concentrations were given a concentration of 100,000 per kilogram of air (approximately 100 L^{-1}), while for TIC-2 simulation the IN concentrations were 5,000 kg^{-1} (approximately 5 L^{-1}). These values were determined based on observations using the CSU continuous flow diffusion chamber of IN. Rogers et al. (2001) measured an average of 85.6 L^{-1} above the inversion, while below the inversion average IN concentrations were measured to be approximately 3 L^{-1}. Based on these values, the concentrations listed above appeared reasonable.

In order to determine the most accurate parameters to use for the control experiment, many simulations were performed by varying specific quantities and then matched up against observations [Figure 3.1]. This section describes the numerous sensitivity experiments performed to accurately reproduce the observed case study. In addition, the effectiveness of the variation in IN concentrations will also be explored.

i. *Condensate percentage*

Initial simulations of PTIC were unsuccessful in reproducing observations and failed to produce any condensate. It was not surprising, however, that RAMS did not produce a cloud due to the fact that it was initialized with a water vapor profile and not total condensate. Because radiosondes are only capable of measuring atmospheric water vapor and they don't saturate, the moisture profile used to initialize RAMS provided a dry bias. To compensate for this in subsequent simulations, additional moisture was added to the vapor profile wherever precipitation was occurring based on Figure 3.1. Following this addition, the simulations produced condensate and matched up reasonably well with observations.

Once RAMS was producing condensate that reproduced the spatial pattern and temporal evolution similar to observations, sensitivity testing commenced. After numerous simulations ranging from 1-15% additional moisture, the percentage that produced the most similar results to observations was 6%.

ii. *CCN variations*

For each IN concentration, three simulations were performed with varying cloud condensation nuclei (CCN) concentrations of 10, 100, and 200 cm^{-3}. There is a direct relationship between CCN concentration and cloud drop concentration, as CCN numbers increase there is a higher probability of forming a cloud drop and thus cloud drop concentrations are higher. With a higher cloud drop concentration at very cold temperatures, then the probability of homogeneous nucleation increases. With each variation in CCN concentration, no change was observed in the results. Because no change took place with variations in CCN concentrations, homogeneous nucleation can be ruled out. If homogeneous nucleation existed, then the pristine ice concentrations would be larger, as liquid water droplets freeze spontaneously into the pristine ice category. The three different concentrations used for sensitivity testing are the values of haze particles that can be potentially activated as CCN, which can more easily freeze, as discussed in the next section.

iii. Homogeneous haze nucleation

Homogeneous nucleation of pure water requires supersaturation with respect to water, which is often fairly difficult to achieve in a wintertime Arctic atmosphere. However, homogeneous nucleation of haze particles is more likely to occur in the Arctic atmosphere because water supersaturation is not necessary. Consequently, RAMS includes a scheme for homogeneous nucleation of haze in which the prescribed concentrations of CCN, given in the previous section, represent the concentrations of haze particles. Although homogeneous haze nucleation is more likely to occur within the wintertime Arctic atmosphere, colder temperatures are required for homogeneous nucleation of haze particles as compared with pure water droplets due to the addition of solute. As a result, RAMS allows homogeneous nucleation of haze particles to take place with temperatures less than -35°C and relative humidity values greater and 82%. Although most of the clouds produced in the simulations occurred with air temperatures greater than -35°C, the upper portions of the atmosphere were within the regime in which homogeneous haze nucleation could be activated. Therefore, it was necessary to determine if this mechanism affected ice production.

Sensitivity testing by turning off this mechanism provided no differences in results, thus the homogeneous nucleation of haze particles did not affect the cloud microphysics. Although the conditions were satisfied, the lack in change of results was likely due to crystals generated from homogenous haze nucleation not exceeding the number of crystals previously activated by IN, as explained in Chapter 2 (N_{id}).

iv. Nudging and linear large-scale tendencies

As described in Chapter 2, two different methods can be used to apply large-scale tendencies, linear large-scale tendencies and large-scale tendencies as nudging. In addition, each method of large-scale tendencies contains an intensity coefficient that can be adjusted to put more emphasis on the observations. Linear tendencies versus nudging as well as the intensity were tested against Figure 3.3 to determine the most accurate parameters for the control experiment.

To begin the sensitivity testing, an intensity of 5% (See α in Equations 8 and 9) was tested for both linear tendencies and nudging. The results between the linear tendencies simulations and the nudging simulations were significantly different and the nudging simulations performed better relative to the observations. To further these results, the intensity of linear tendencies was varied from 0.5% up to 25%. For each set of simulations the results were relatively similar, however different from radar observations. These results rule out linear large-scale tendencies for providing the most realistic control experiment.

After ruling out linear large-scale tendencies as the primary method for incorporating observations, testing of nudging ensued. First, nudging intensity was varied from 0.01% to 25%. The results were very similar in the nudging intensity range of 1% though 25%, and the most dissimilar from 0.01% through 1%. This meant that observations were masking the changes governed by small-scale features that were resolved by the nudging intensity over 1%, therefore choosing a nudging intensity less than 1% would be able to keep the small-scale features while also incorporating the larger-scale forcing. As the model progresses the dependence on observation builds with time, therefore it was thought that using a higher nudging intensity during spinup time would allow the model to more efficiently develop a distribution of eddies. This increase in nudging intensity during spinup was tested by varying the nudging intensity for the first hour between 1% and 25% and then decreasing the intensity to 0.1%, as this intensity provided the most significant results. In performing the sensitivity tests, the simulation in which a nudging intensity of 5% for the first hour and 0.1% for the remainder of the simulation provided the most accurate results relative to radar observations, as well as the most significant differences between IN concentrations. The next section describes the results of the control experiment.

3.3 Results

After numerous sensitivity tests, the control experiment was created with large-scale tendencies as nudging with a first-hour intensity of 5% and a remaining intensity of 0.1%. As explained in Chapter 1, it is more likely to have a larger number of small particles for the simulation with high concentrations. For the low IN concentrations, the larger particles will grow large enough, via less competition of available vapor, to precipitate out and dehydrate the atmosphere. For the remainder of this paper, the high IN concentration simulation will be referred to as PTIC-h, while the low IN concentration simulation will be referred to as PTIC-l. This section presents all results pertaining to PTIC while the following section provides the discussion. It is of note that because TIC's occur above the inversion, all data presented are greater than or equal to 1km AGL.

While the PTIC event occurred continuously from 7 Jan through 8 Jan, there are two main peaks in intensity. As shown in Figure 3.1, the first peak occurred on the 7^{th}. Initially, the strongest reflectivity values (-20+ dBZ) extended up to 4 km, however after about 4 hours the cloud top heights dropped to 3 km. This first peak in intensity, herein named Area 1, lasted approximately 12 hours and then dropped off for approximately 10 hours. On the 8^{th}, the reflectivity values again increased in intensity with values greater than -20 dBZ and lasted for approximately 12 hours. This second peak in radar reflectivity, herein named Area 2, contained stronger reflectivity values than Area 1 and lasted approximately 18 hours, however only extended up to 3 km. These two Areas were well represented in the results of the control experiment.

The results from the RAMS simulations of the control experiment are shown below. The temporal and spatial distribution of pristine ice can be seen in Figure 3.6, which shows the mean mass diameter of pristine ice for both IN concentrations. The data are displayed in a time versus height format for effective comparison with observed radar data. Both Area 1 and Area 2 are clearly distinguishable with peaks in effective diameter occurring around 12Z on both the 7th and 8th. The depth of the ice cloud is similar to radar observations in that Area 1 extends up to 4km, while Area 2 extends up to 3 km. PTIC-h clearly shows smaller pristine diameters than PTIC-l (Figure 3.6). Area 1 demonstrates the most significant differences in diameters with maximum values at 3km of approximately 60μm and 120μm for the high and low IN simulations, respectively. In addition, Area 2 contained differences in pristine ice diameters, however the difference was significantly lower than Area 1 with maximum values on the order of 20μm different. With respect to these results, Area 1 appears to support the hypothesis that a reduction in IN concentration causes larger crystal growth and thus deserved a closer look into the microphysics.

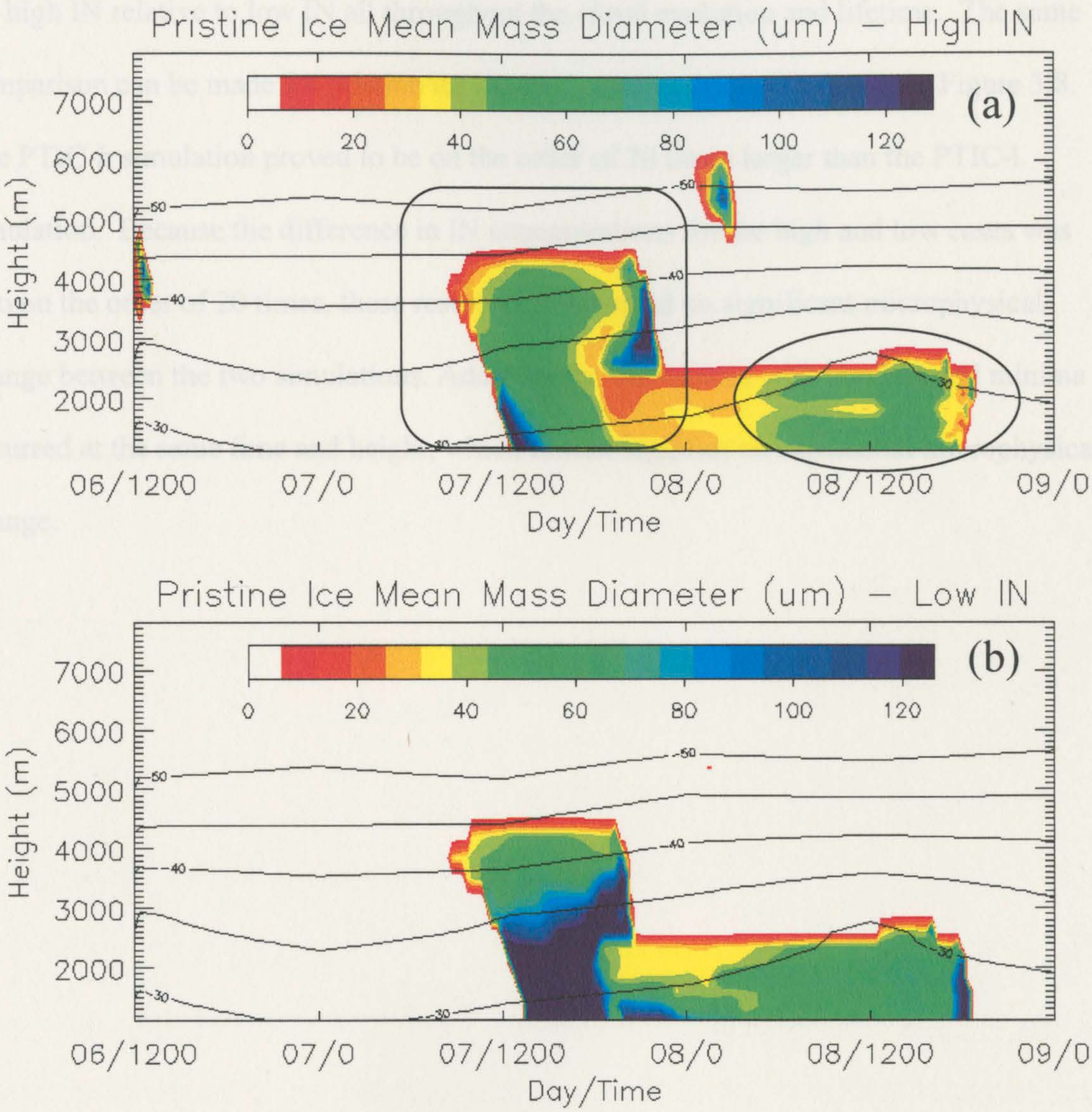

Figure 3.6: Pristine ice mean mass diameter (in μm) for the high IN simulation (a) and the low IN simulation (b). The square depicts the region for Area 1, while the oval shows the region for Area 2. Ambient air temperature is depicted by black contours.

Looking at pristine ice mixing ratios and number concentrations should present a clearer picture of the cloud makeup. Figure 3.7 shows the pristine ice mixing ratios for high and low IN concentrations. Once again, Areas 1 and 2 are clearly distinguishable with Area 2 providing the densest cloud, similar to radar observations. When comparing the two IN concentration simulations, the mixing ratios are approximately 20 times larger for high IN relative to low IN all throughout the cloud evolution and lifetime. The same comparison can be made for pristine ice number concentrations, as shown in Figure 3.8. The PTIC-h simulation proved to be on the order of 20 times larger than the PTIC-l simulation. Because the difference in IN concentrations for the high and low cases was also on the order of 20 times, these results demonstrated no significant microphysical change between the two simulations. Additionally, the regions with maxima and minima occurred at the same time and height, which further signifies no substantial microphysical change.

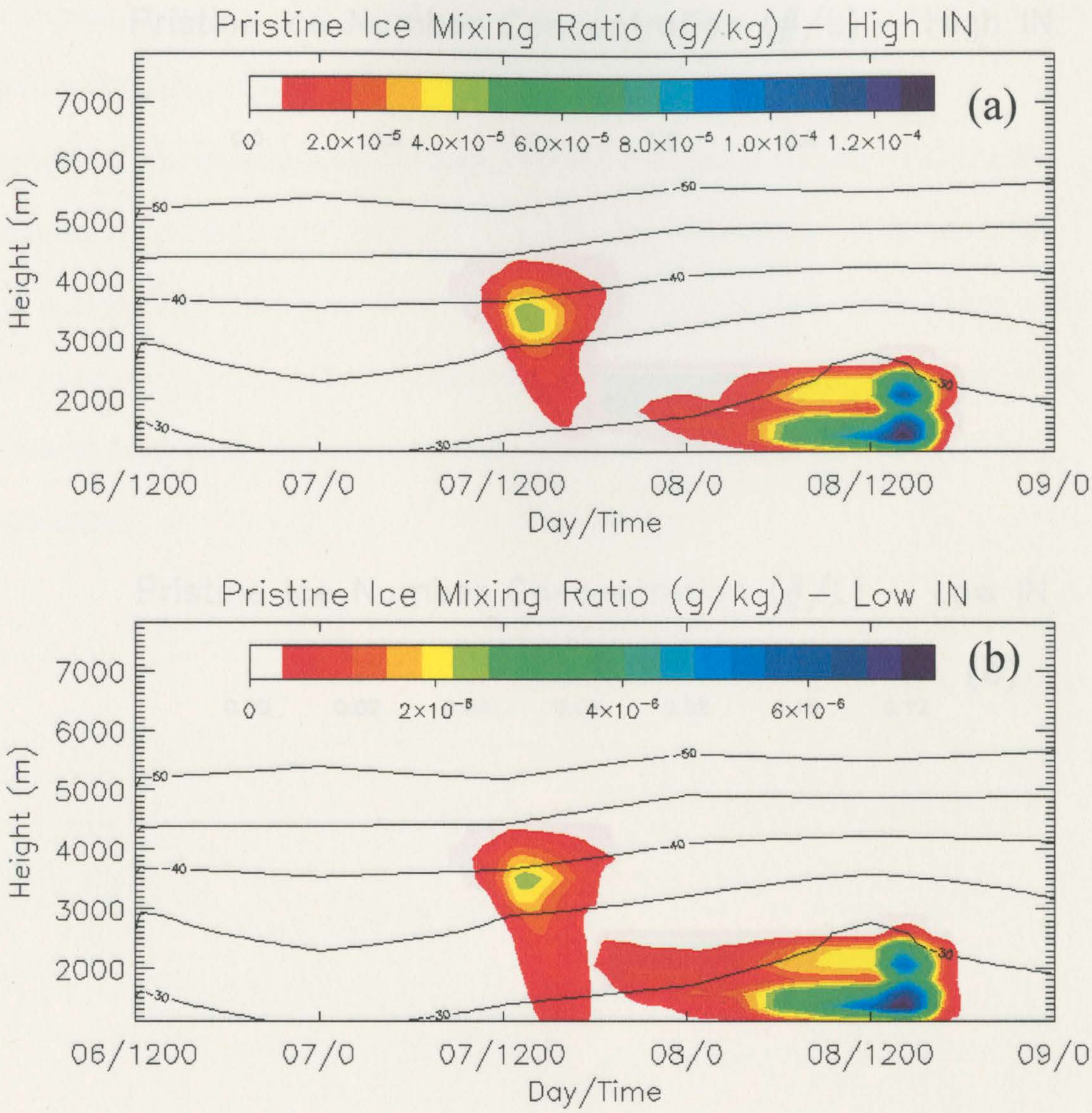

Figure 3.7: Pristine ice mixing ratios (in g/kg) for the high IN simulation (a) and the low IN simulation (b). Ambient air temperature is depicted by black contours.

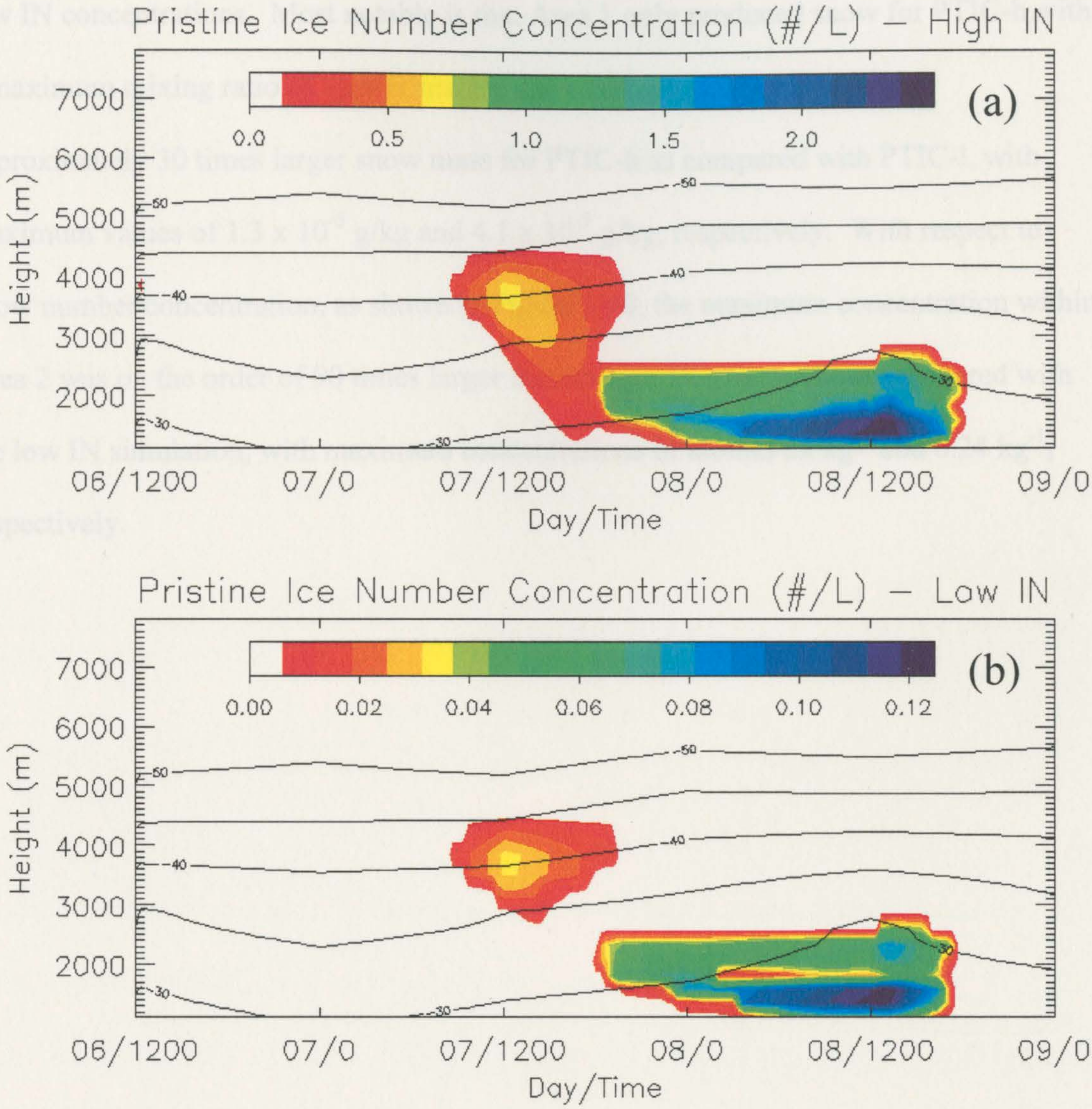

Figure 3.8: Pristine ice number concentrations (in #/kg) for the high IN simulation (a) and the low IN simulation (b). Ambient air temperature is depicted by black contours.

Within RAMS pristine ice is allowed to sedimentate, however their terminal velocities are significantly smaller than for snow and aggregates. Therefore it is important to examine both snow and aggregate categories, as they usually contribute more to sedimentation, to observe which case contributes most significantly to dehydration of the atmosphere. Figure 3.9 shows the snow mixing ratio for both high and low IN concentrations. Most notable is that Area 1 only produced snow for PTIC-h with a maximum mixing ratio of approximately 2.0 x 10^{-6} g/kg. Area 2 contained approximately 30 times larger snow mass for PTIC-h as compared with PTIC-l, with maximum values of 1.3 x 10^{-5} g/kg and 4.1 x 10^{-7} g/kg, respectively. With respect to snow number concentration, as shown in Figure 3.10, the maximum concentration within Area 2 was on the order of 90 times larger for the high IN simulation as compared with the low IN simulation, with maximum concentrations of around 22 kg^{-1} and 0.24 kg^{-1}, respectively.

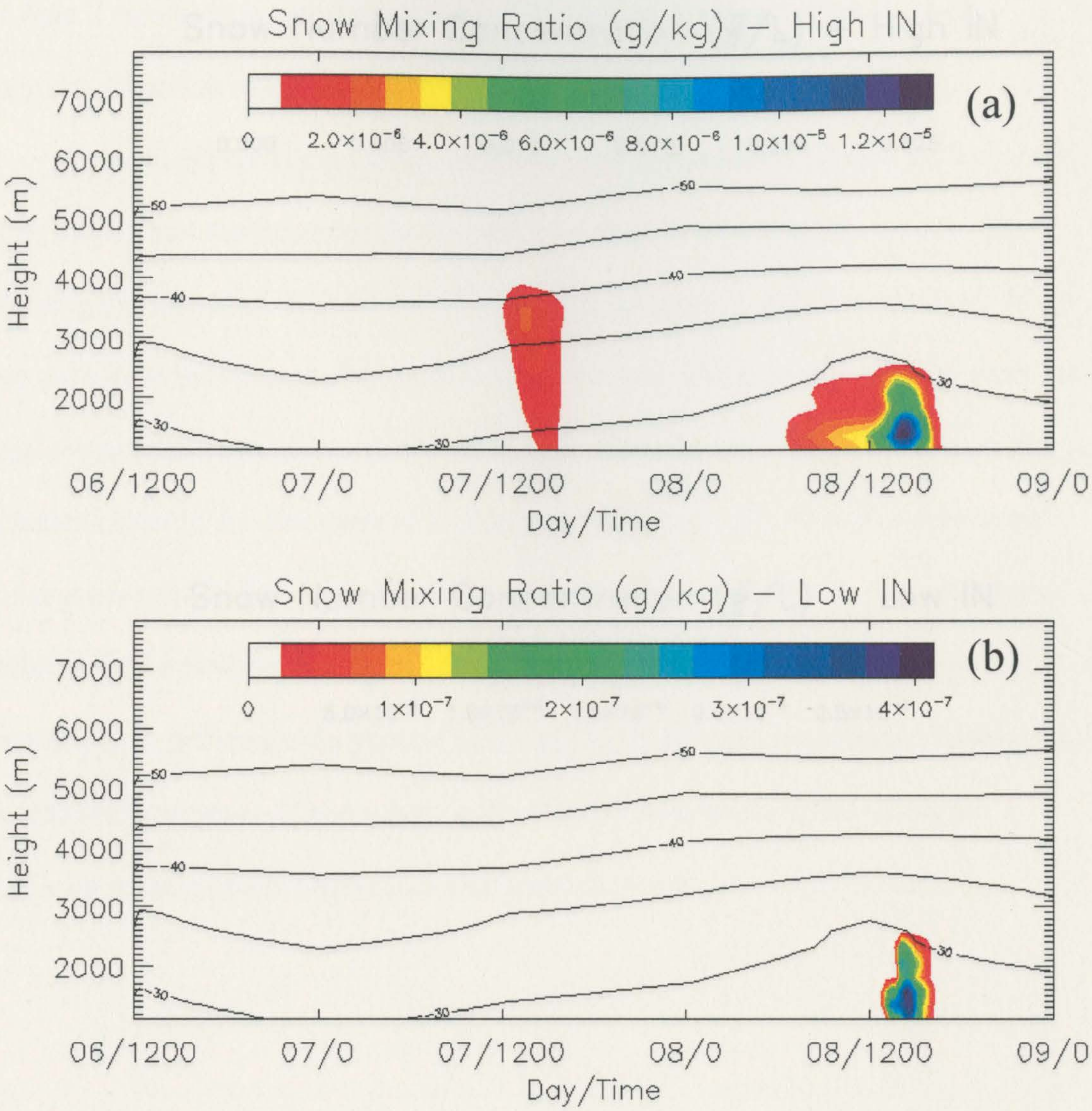

Figure 3.9: Snow mixing ratios (in g/kg) for the high IN simulation (a) and the low IN simulation (b). Ambient air temperature is depicted by black contours.

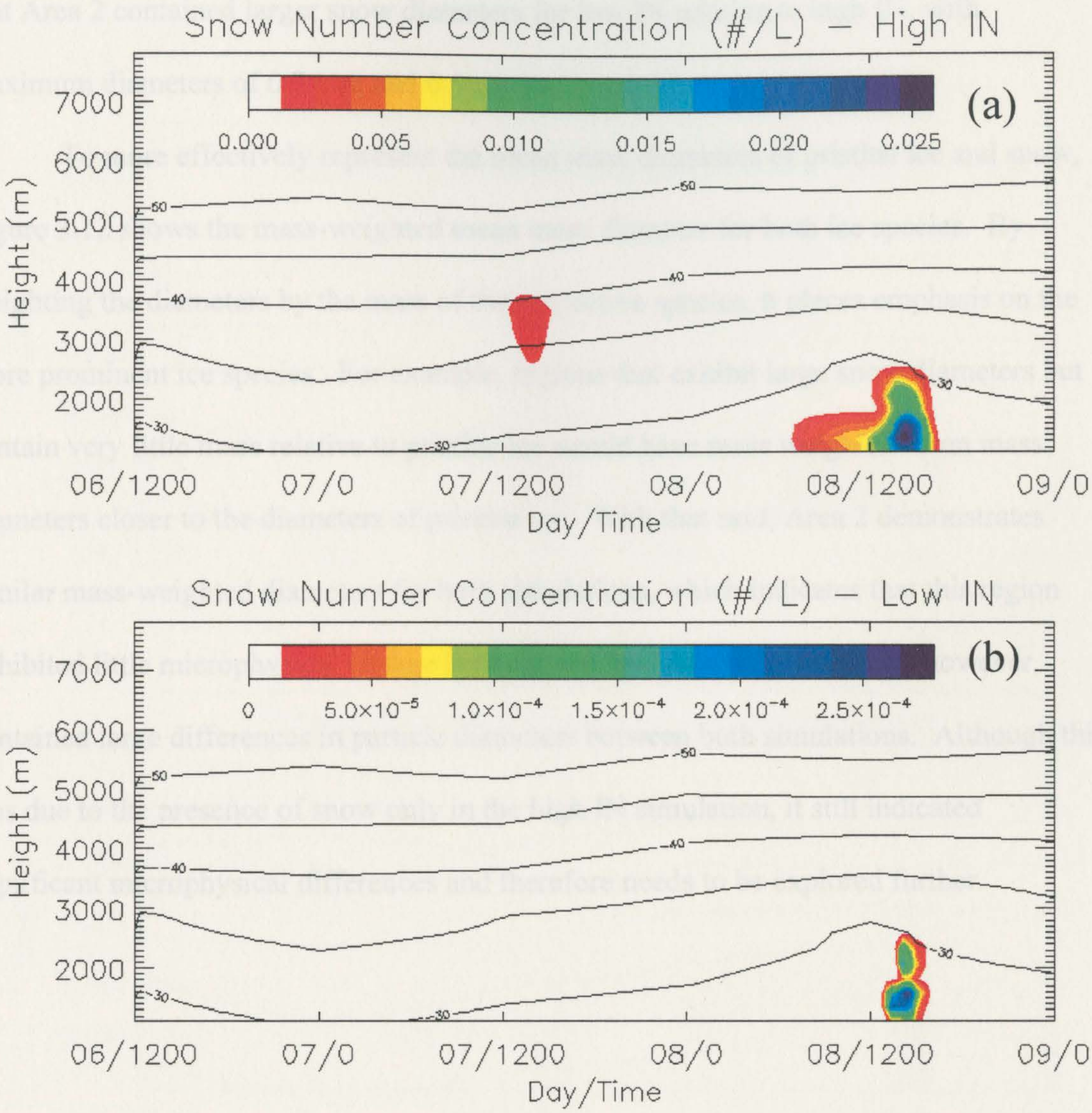

Figure 3.10: Snow number concentration (in #/kg) for the high IN simulation (a) and the low IN simulation (b). Ambient air temperature is depicted by black contours.

Because the difference in mixing ratios were significantly smaller than the differences in number concentration, it would suggest that the snow diameters should be larger for PTIC-l as compared with PTIC-h. Figure 3.11 illustrates the mean mass diameters for snow for both simulations. As deduced by Figures 3.9 and 3.10, Figure 3.11 also shows that Area 2 contained larger snow diameters for low IN relative to high IN, with maximum diameters of 0.7 mm and 0.5 mm, respectively.

To more effectively represent the mean mass diameters of pristine ice and snow, Figure 3.12 shows the mass-weighted mean mass diameter for both ice species. By weighting the diameters by the mass of the respective species, it places emphasis on the more prominent ice species. For example, regions that exhibit large snow diameters but contain very little mass relative to pristine ice would have mass weighted mean mass diameters closer to the diameters of pristine ice. With that said, Area 2 demonstrates similar mass-weighted diameters for both simulations, which indicates that this region exhibited little microphysical change between the two simulations. Area 1 however, contained large differences in particle diameters between both simulations. Although this was due to the presence of snow only in the high IN simulation, it still indicated significant microphysical differences and therefore needs to be explored further.

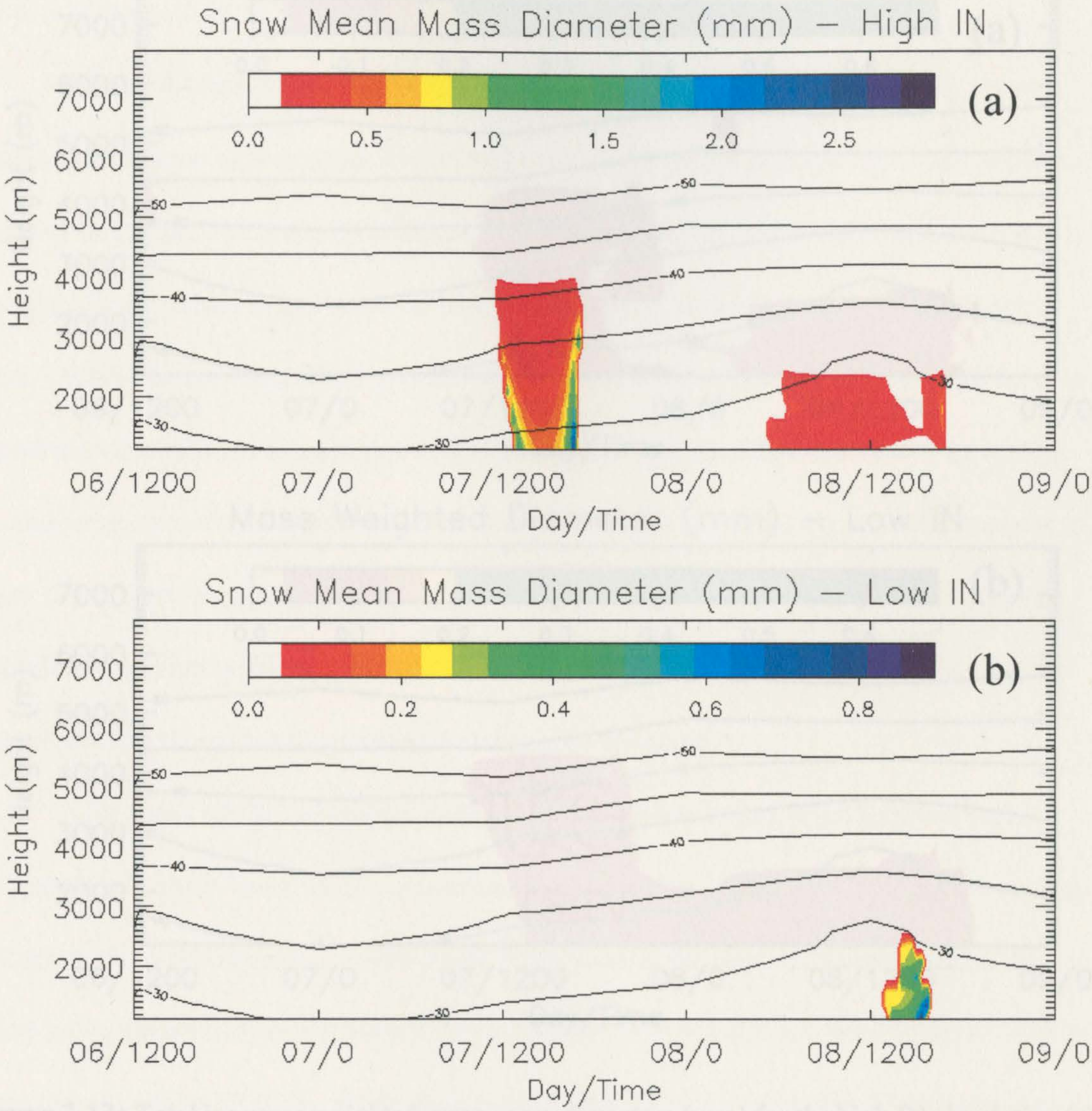

Figure 3.11: Snow mean mass diameters (in mm) for the high IN simulation (a) and the low IN simulation (b). Ambient air temperature is depicted by black contours.

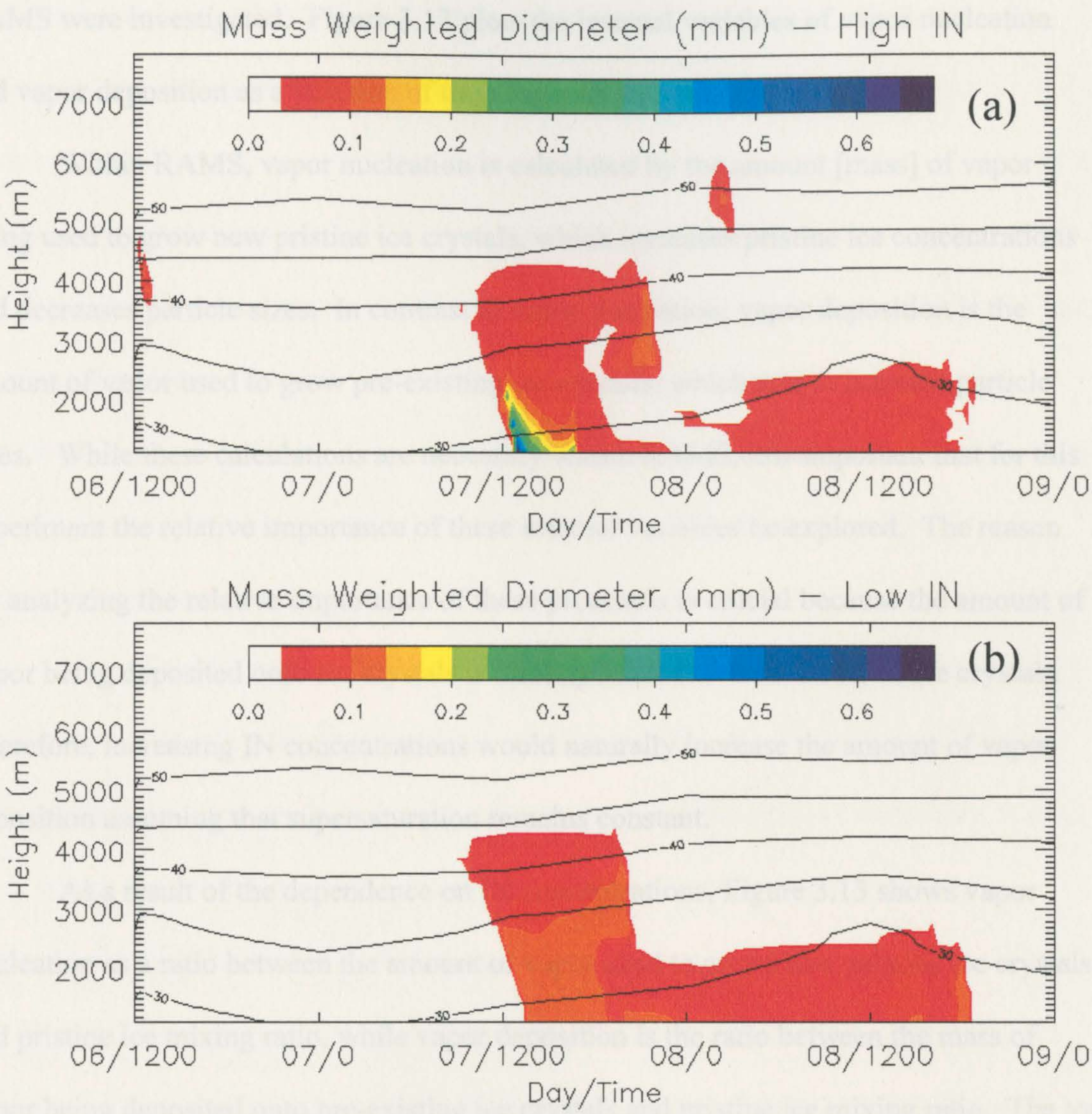

Figure 3.12: Total ice mass weighted mean mass diameters (mm) for the high IN simulation (a) and the low IN simulation (b). Ambient air temperature is depicted by black contours.

In addition to snow and pristine ice, aggregates also contribute to sedimentation and consequently dehydration of the atmosphere, however no aggregates were produced from either simulation. Therefore, further investigation of only snow and pristine ice was required. To understand the microphysics involved with PTIC, internal variables within

RAMS were investigated. Figure 3.13 plots the internal variables of vapor nucleation and vapor deposition as a function of time for both IN simulations.

Within RAMS, vapor nucleation is calculated by the amount [mass] of vapor being used to grow new pristine ice crystals, which increases pristine ice concentrations and decreases particle sizes. In contrast to vapor nucleation, vapor deposition is the amount of vapor used to grow pre-existing ice crystals, which acts to increase particle sizes. While these calculations are necessary within RAMS, it is important that for this experiment the relative importance of these internal variables be explored. The reason for analyzing the relative importance of these processes is crucial because the amount of vapor being deposited onto ice crystals is directly related to the number of ice crystals. Therefore, increasing IN concentrations would naturally increase the amount of vapor deposition assuming that supersaturation remains constant.

As a result of the dependence on IN concentrations, Figure 3.13 shows vapor nucleation as a ratio between the amount of vapor used to create new pristine ice crystals and pristine ice mixing ratio, while vapor deposition is the ratio between the mass of vapor being deposited onto pre-existing ice crystals and pristine ice mixing ratio. The top plot corresponds to PTIC-h, while the bottom is for PTIC-l. As means for comparison, each plot also shows the maximum pristine ice concentration at each time. Both Area 1 and 2 can be seen in Figure 3.13 by the areas of higher vapor deposition fraction. As the fraction of vapor nucleation decreases, the fraction of vapor deposition increases in response to the availability of vapor. For Area 1, the region of vapor deposition was slightly larger for PTIC-l as compared with PTIC-h, albeit the difference was not significant. This suggests that there was a slight increase in the fraction of vapor deposited onto ice crystals, which leads to larger particles that could potentially sedimentate and act to dehydrate the atmosphere. The same can be said of Area 2, however the difference in total vapor deposition fraction was even smaller. Within Area 1, it is of note that the pristine ice concentration began to decline approximately 6 hours earlier for PTIC-l as compared with PTIC-h results. This likely suggests that for the low IN simulation supersaturation was not sufficient to sustain all crystals, despite the increase in vapor deposition. Conversely for the high IN simulation, supersaturation was sufficient to sustain most ice crystals and the small fraction of vapor nucleation was efficiently used in creating additional ice crystals.

To explain the previously mentioned characteristics, Figure 3.14 illustrates the stratification of pristine ice concentration. For the high IN simulation, the pristine ice concentration increases with increasing altitude, however the peak concentration at each level occurs further in time with decreasing altitude. This signature may allude to sedimentation fall streaks of pristine ice crystals. This same process can be seen in the low IN simulation, however the concentrations deplete by 2733m AGL. These results indicate that the supersaturation levels below approximately 3 km were insufficient to sustain the ice crystals. It is also of note that the peak concentrations of pristine ice decreased with decreasing altitude for the high IN simulation, however this was mainly due to a water species conversion into the snow category, as shown by the snow concentrations in Figure 3.14. Conversely, this did not occur for the low IN simulation, as there was no snow present for Area 1.

For Area 2, the vapor deposition and vapor nucleation appeared very similar for both simulations. In addition, the stratification of both pristine ice and snow showed little differences, therefore there was no further examination of Area 2.

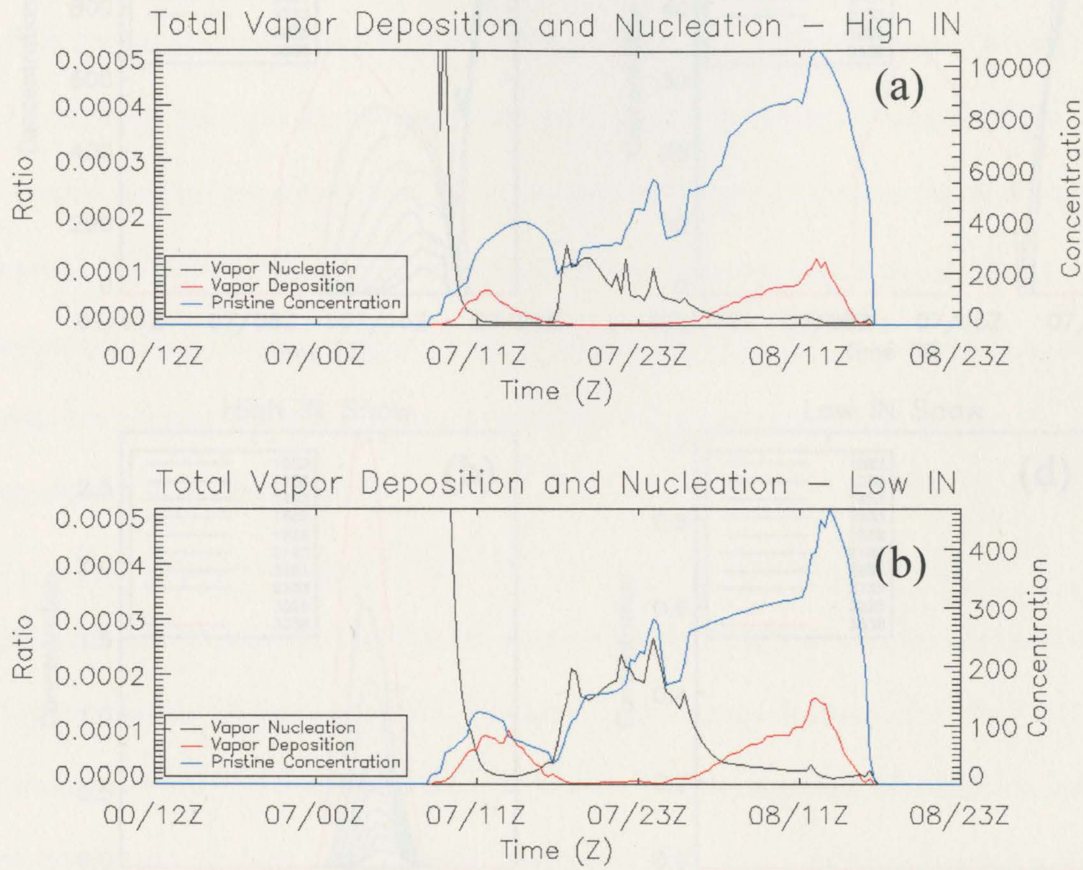

Figure 3.13: Curves for total vapor deposition fraction, total vapor nucleation fraction, and maximum pristine ice concentrations for: (a) High IN simulation, and (b) Low IN simulation.

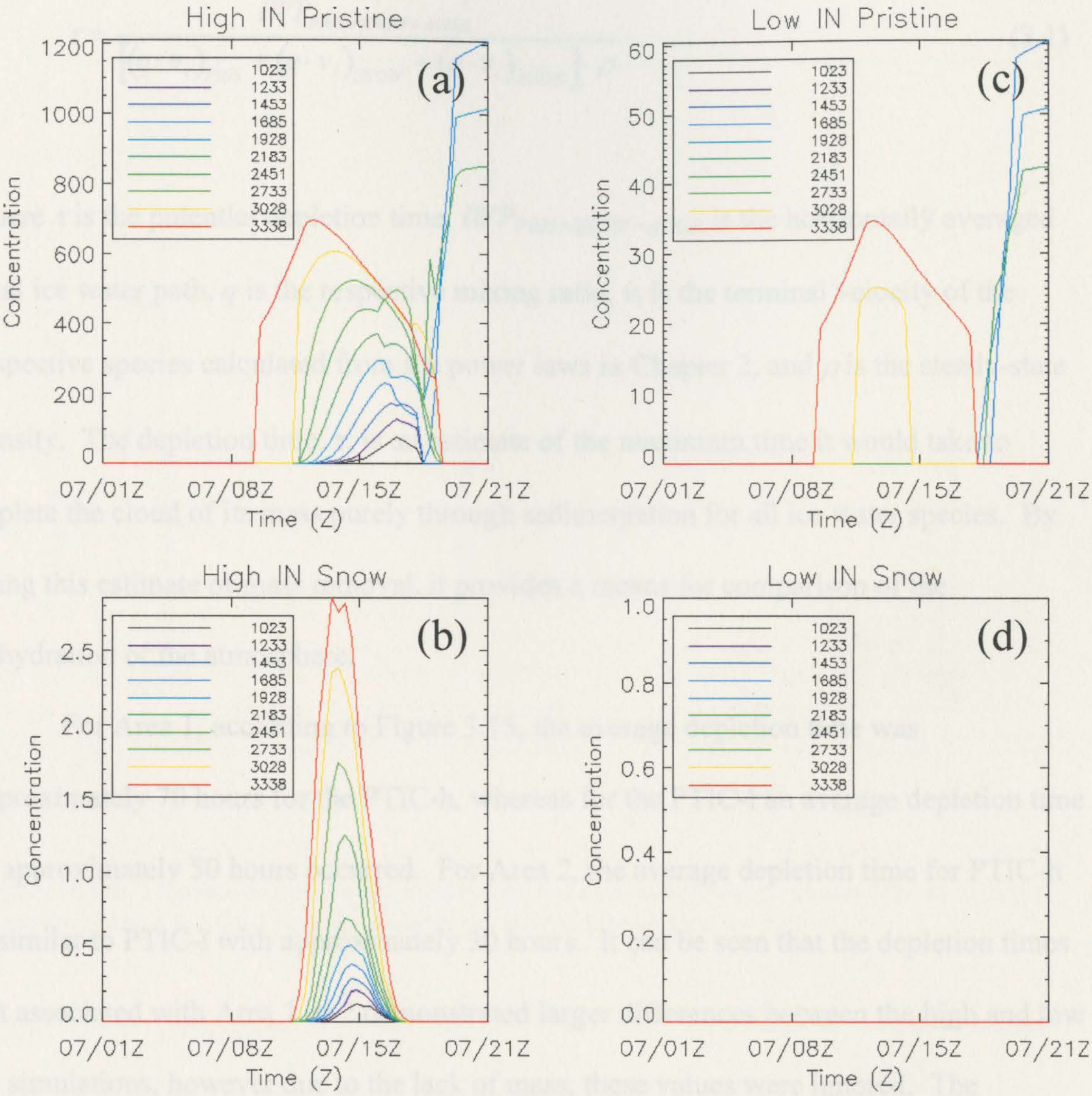

Figure 3.14: Curves of horizontally averaged concentrations versus time for various levels (m) above the boundary layer for Area1. (a) High IN simulation with pristine concentrations (L^{-1}). (b) High IN simulation with snow concentrations (L^{-1}). (c) Low IN simulation with pristine concentrations (L^{-1}). (d) Low IN concentrations with snow concentrations (L^{-1}).

In an effort to quantify the potential dehydration for both simulations, Figure 3.15 illustrates the potential depletion time of the cloud, which is shown below by Equation 3.1:

$$\tau = \frac{IWP_{PRIS+SNOW+AGGR}}{\left[(q \cdot v_t)_{PRIS} + (q \cdot v_t)_{SNOW} + (q \cdot v_t)_{AGGR}\right] \cdot \rho} \quad (3.1)$$

where τ is the potential depletion time, $IWP_{PRIS+SNOW+AGGR}$ is the horizontally averaged total ice water path, q is the respective mixing ratio, v_t is the terminal velocity of the respective species calculated from the power laws in Chapter 2, and ρ is the steady-state density. The depletion time, τ, is an estimate of the maximum time it would take to deplete the cloud of its mass purely through sedimentation for all ice water species. By using this estimate of mass removal, it provides a means for comparison of the dehydration of the atmosphere.

For Area 1, according to Figure 3.15, the average depletion time was approximately 70 hours for the PTIC-h, whereas for the PTIC-l an average depletion time of approximately 50 hours occurred. For Area 2, the average depletion time for PTIC-h is similar to PTIC-l with approximately 30 hours. It can be seen that the depletion times not associated with Area 1 or 2 demonstrated larger differences between the high and low IN simulations, however due to the lack of mass, these values were ignored. The decreased depletion time for Area 1 indicates that a higher fraction of the cloud is comprised of larger sedimentating particles with low IN as compared with high IN. Therefore, the low IN simulation for Area 1 had a greater likelihood of atmospheric dehydration.

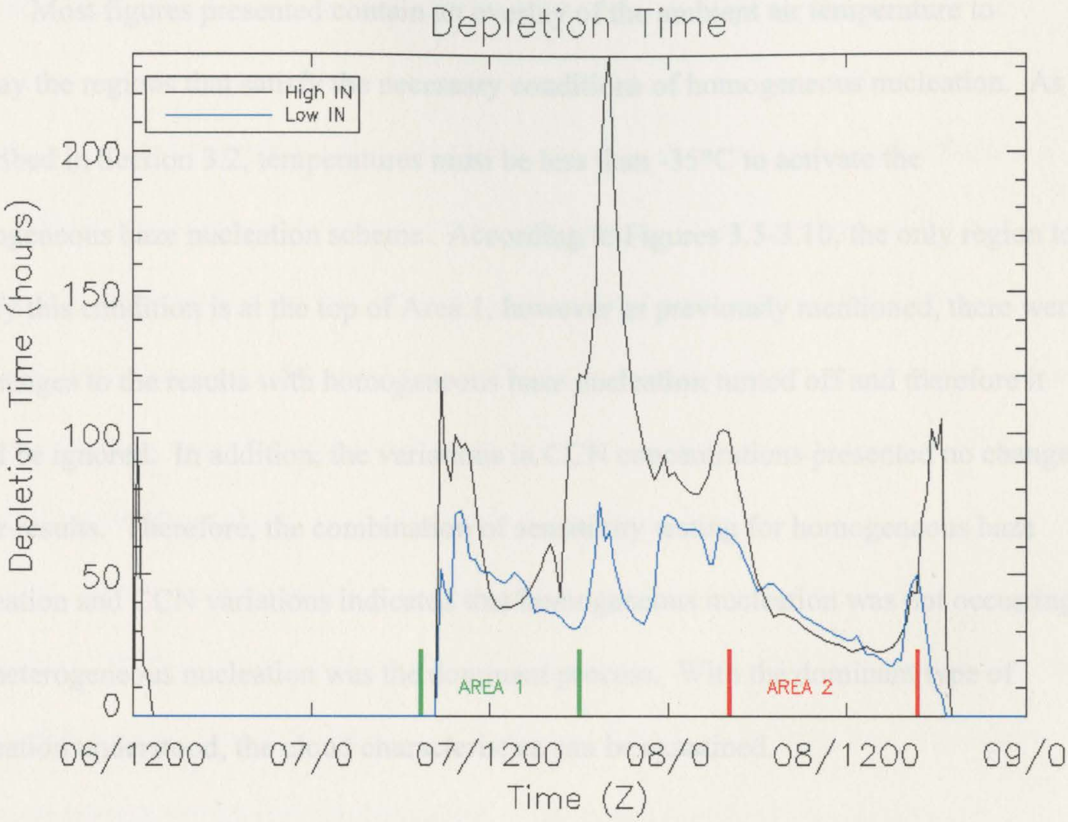

Figure 3.15: Depletion time versus model time for both simulations. Green lines denote the boundary times for Area 1, while the red lines are the boundaries for Area 2.

3.4 Discussion

The results presented above do not clearly suggest that a decrease in active IN concentrations promote larger crystal growth that act to dehydrate the Arctic atmosphere. Although there were some conflicting results, the overall outcome for both Area 1 and 2 showed a lack in significant change between high and low IN concentrations. This discussion will analyze Areas 1 and 2 separately, as each exhibited relatively different behaviors with Area 1 providing the most significant microphysical differences between the two simulations.

Most figures presented contain an overlay of the ambient air temperature to portray the regions that satisfy the necessary conditions of homogeneous nucleation. As described in Section 3.2, temperatures must be less than -35°C to activate the homogeneous haze nucleation scheme. According to Figures 3.5-3.10, the only region to satisfy this condition is at the top of Area 1, however as previously mentioned, there were no changes to the results with homogeneous haze nucleation turned off and therefore it could be ignored. In addition, the variations in CCN concentrations presented no change in the results. Therefore, the combination of sensitivity testing for homogeneous haze nucleation and CCN variations indicated that homogeneous nucleation was not occurring and heterogeneous nucleation was the dominant process. With the dominant type of nucleation understood, the cloud characteristics can be examined.

3.4.1 Area 1

Overall, this area, defined by the 12 hour long maximum in observed radar reflectivity, produced the greatest microphysical differences between the high and low IN simulations. With respect to pristine ice, the mixing ratios and number concentrations between the two simulations were of the same ratio as compared with the respective ratio of IN concentrations. This suggests that the linear changes in mass and concentration of pristine ice for PTIC-h as compared with PTIC-l is solely a result of similar linear changes in the initial IN concentrations and not of microphysical change. Conversely, the pristine ice mean mass diameters contained differences on the order of twice as large for the low IN simulation. These large differences in pristine ice diameters between the two simulations should suggest atmospheric dehydration via sedimentation for PTIC-l due to large crystal growth. However, the location in which the large differences in diameters occurred contained relatively little mass, therefore these diameter differences were of little value to the dehydration of the atmosphere. The combination of a lack in nonlinearity between mixing ratios and number concentration versus IN variation concentrations along with the maximum difference in pristine ice crystal diameter located in a region of low mass indicated that the cloud make-up did not show signs of IN change dehydrating the atmosphere.

In addition to pristine ice, snow was also observed in the results of the simulations. With pristine ice diameters generally larger for the low IN simulation, it was expected that snow diameters should also be larger. This was far from true, as no snow was even present for the low IN simulation. The reason for this is that pristine ice crystals sedimentated into a region with lower supersaturation, thus causing the pristine ice crystals to sublimate. The evidence of this process was shown in the results in two ways: 1) As vapor deposition increased, maximum pristine concentration decreased, and 2) With decreasing altitude, pristine concentration also decreased and became nonexistent below about 2800m.

To further quantify the dehydration of the atmosphere, mass depletion time was calculated. It showed that for Area 1, the low IN simulation could potentially deplete the cloud of its mass quicker than for the high IN simulation. Thus, the dehydration effect could potentially take place. Although the depletion time for Area 1 indicated a difference between the two simulations, the difference in depletion time was not large enough to override the other data.

As such, due to the relatively insignificant changes in pristine ice and the lack of snow for the low IN simulation, it was determined that Area 1 did not demonstrate enough qualities of atmospheric dehydration by reducing the amount of active IN to support the hypothesis.

3.4.2 Area 2

This region was defined by the second maximum in observed radar reflectivity that lasted approximately 18 hours. Similar to Area 1, this area demonstrated no significant change in the ratios between the high and low IN simulations for both mixing ratios and number concentrations versus the ratio in the respective IN concentrations. However unlike Area 1, this area demonstrated lower maximum differences in pristine diameters. The smaller difference in pristine diameters combined with the described trend in mixing ratios and number concentrations indicated no significant microphysical change between the two simulations with respect to pristine ice.

Unlike pristine ice, the snow make-up within Area 2 did contain non-linear differences between the two simulations. Mixing ratios were on the order of 30 times larger while number concentrations were on the order of 90 times larger for the high IN simulation as compared with the low IN simulation. This nonlinearity suggested that the snow diameters should be larger for the IN simulation, which was confirmed with a difference in maximum snow effective diameters of approximately 0.2mm in favor of the low IN simulation.

With snow being a factor along with pristine ice, a more accurate measure of particle size was needed. Therefore, mass-weighted diameters of total ice were generated. They showed that the snow provided little significance with respect to the cloud as a whole, as the mass weighted diameters had little variation between the two simulations. Therefore, the differences in both simulations with respect to snow did not appear to be significant with respect to the overall cloud.

To further quantify the effect of pristine ice and snow on the dehydration of the atmosphere, mass depletion time was calculated. It showed that for Area 2, there was virtually no change in depletion time. Thus, the potential dehydration for the low IN simulations was not larger than for the high IN simulations. As such, Area 2 did not demonstrate any microphysical change with respect to both pristine ice and snow.

In summary, the PTIC case simulated by RAMS with two difference IN concentrations did not provide enough evidence to prove that this case study contained atmospheric dehydration effects. In addition to possible limitations of the model, the model was driven by observations that also might contain errors, especially because the Arctic winter atmosphere contains such small amounts of vapor that radiosonde errors can become very large. Therefore, it was thought to explore conditions within a reasonable range that could maximize the results in support of a TIC-2 event. The use of PTIC as a benchmark to overcome uncertainties will be presented and explored in the following section as a sensitivity experiment.

CHAPTER 4

SENSITIVITY EXPERIMENT

As illustrated in the previous chapter, RAMS simulations of the PEARL Thin Ice Cloud (PTIC) case study did not provide concrete evidence that a decrease in IN concentrations would act to grow crystals large enough to sedimentate and dehydrate the atmosphere. Due to the inconclusive results combined with known uncertainties in the measurements of radiosonde observations, a sensitivity experiment was designed to examine the environmental conditions that maximize the results of Thin Ice Clouds. This chapter will describe in detail the structure of this sensitivity experiment, the model setup used, the results of the simulations, and a concluding discussion.

4.1 Experimental Setup

As explained in Chapter 3, Area 1 was characterized by the 12 hour maximum in radar reflectivity values on the January 7th. This timeframe demonstrated the most significant microphysical differences between PTIC-h and PTIC-l. PTIC-l produced pristine ice crystals approximately twice as large as PTIC-h. Additionally, PTIC-l had slightly increased vapor deposition fraction values. Although Area 1 did not produce snow for PTIC-l, it was likely due to decreased supersaturation lower in the cloud. With a theoretical increase in supersaturation, Area 1 could potentially demonstrate more significant results for the removal of mass from the atmosphere, thus atmospheric dehydration. Area 2, however, did not show significant changes between PTIC-h and PTIC-l in particle diameters for both pristine ice and snow and was therefore considered to be less representative of TIC's. For these reasons, the time at which Area 1 occurred was chosen as the benchmark for the sensitivity experiment.

In order to determine the atmospheric conditions that maximize the characteristics of a TIC-2 event, an experiment was created with sensitivity on the initial environmental conditions. As previously mentioned, Area 1 demonstrated the most promising signs of a TIC-2 event, therefore the radiosonde observation profile used for this experiment was 7 January 2007 12Z, herein named BSPTIC (Benchmark Sounding for PEARL Thin Ice Clouds) which occurred in the temporal center of Area 1. Figure 4.1 shows the thermodynamic profiles of the benchmark sounding.

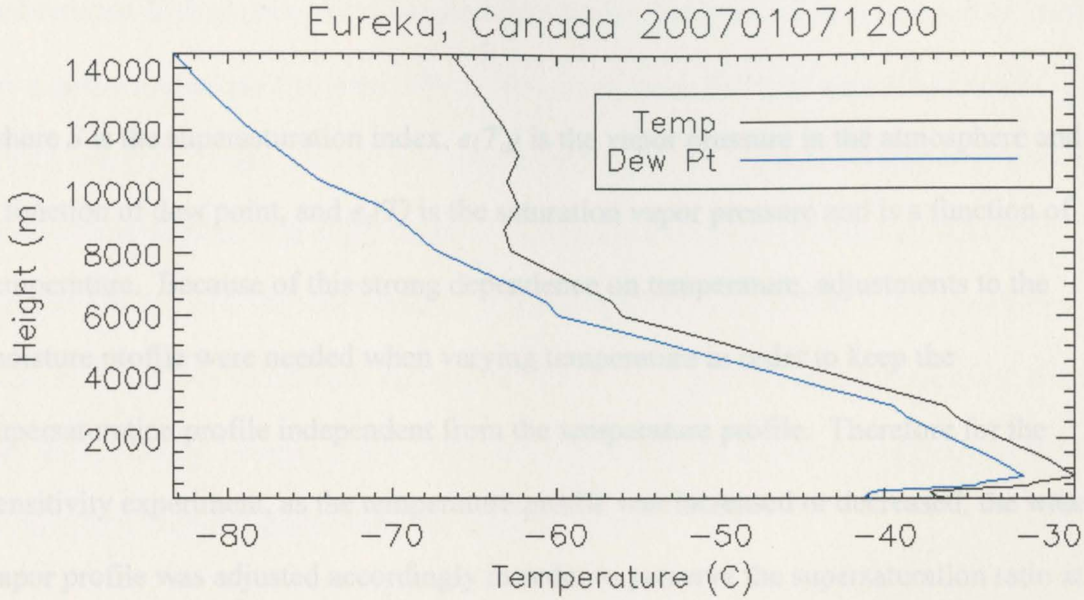

Figure 4.1: Temperature and dew point profiles for the sounding used as the benchmark for the sensitivity experiment that occurred on 7 Jan 2007 at 12Z. The arctic inversion can be seen below approximately 1km.

Three environmental variables are used for the input sounding within RAMS: temperature, moisture, and wind. For this sensitivity experiment, the temperature and moisture profiles were varied independently. Although these two atmospheric quantities vary independently in the atmosphere, they are related with respect to cloud formation due to saturation. For example, as temperature increases with a fixed amount of moisture, relative humidity decreases which moves the atmosphere further from cloud formation. Due to this process, the moisture profile used in the sensitivity experiment was supersaturation (i.e. relative humidity when below 1.00). Supersaturation, however, is strongly dependent on temperature, as shown by

$$S = \frac{e(T_d)}{e_s(T)} \tag{4.1}$$

where S is the supersaturation index, $e(T_d)$ is the vapor pressure in the atmosphere and is a function of dew point, and $e_s(T)$ is the saturation vapor pressure and is a function of temperature. Because of this strong dependence on temperature, adjustments to the moisture profile were needed when varying temperature in order to keep the supersaturation profile independent from the temperature profile. Therefore for the sensitivity experiment, as the temperature profile was increased or decreased, the water vapor profile was adjusted accordingly in order to preserve the supersaturation ratio at each level. Thus, the sensitivity experiment consisted of making initial condition modifications to the BSPTIC temperature and supersaturation profiles independently. With the atmospheric quantities to be varied determined, the structure of the experiment was needed.

To determine the range for adjusting the temperature profile, the surface temperatures for the entire case study (6 Jan 12Z to 9 Jan 00Z) were compared against one another. The maximum variation between surface temperatures was approximately 5°C. As a result, the temperature profiles for the sensitivity experiment had maximum variations for the entire profile of 5°C and -5°C off of BSPTIC. With a range of 10°C, it was chosen that the temperature profile spread between simulations would be 1°C, which equated to eleven distinct temperature profiles.

For the deviations in the supersaturation profiles, it was preferred to vary by percentages. Due to the nature of the TIC-2 events, high supersaturations within the clouds are required to rapidly form ice crystals and therefore more emphasis was placed on simulations with higher supersaturation percentages. Additionally, the supersaturation percentages were varied within a reasonable range. Therefore, it was selected to fluctuate the supersaturation profile from -4% to 10% away from BSPTIC with 2% intervals, which resulted in eight successive supersaturation profiles. The combination of eleven temperature profiles with eight supersaturation profiles yields 88 different RAMS simulations for each IN concentration. Similar to PTIC-h and PTIC-l, this sensitivity experiment will initialize each batch of 88 simulations with IN concentrations of 100,000 kg^{-1} and 5,000 kg^{-1}, respectively. With the structure of the experiment explained, the next section describes the model setup for each simulation.

4.2 RAMS Setup

The general simulation conditions for each simulation within the sensitivity experiment are very similar to the setup of the PEARL case study described in Chapter 3. This similarity was chosen mainly for straightforward comparison and computational efficiency, as 176 simulations were performed. This section describes the RAMS setup for each simulation of the sensitivity experiment.

RAMS was configured as a CRM that can be seen as a single column model capable of resolving the turbulent eddies containing most of the energy. The 2-dimensional model, similar to PTIC simulations, was set to 100m grid spacing and was 10km long. There were 47 vertical levels that emphasized the boundary layer and cloud layer; elsewhere the vertical resolution was relatively coarser. A 3s timestep was used and the model was allowed to run for 60 hours.

Table 4.1: Chart of framework settings used in all sensitivity experiment simulations.

Framework Aspect	Setting
Model configuration	Two-dimensional, single grid cloud resolving model
Horizontal grid	100 m grid spacing 100 horizontal grid points
Vertical grid	47 vertical levels Variable grid spacing with emphasis on boundary layer and cloud layer
Timestep	3 seconds
Simulation length	60 hours

Each run used the level 3, two-moment microphysics scheme, meaning that mixing ratios and number concentrations for all hydrometeor species were prognosed. Table 4.1 lists the major input parameters used for initialization of each simulation. It can be seen that the input parameters are identical to the simulations of the PEARL case study, however unlike the PTIC simulations the sensitivity experiment did not use any form of large-scale linear tendencies. Because the goal of the study was to see which environmental conditions maximized the characteristics of a TIC-2 event, no atmospheric information was needed other than the initial conditions.

Overall, this sensitivity experiment consisted of two batches of simulations: one for the high IN concentration and one for the low IN concentration. Each batch contained 88 simulations in which there were combinations between eleven temperature profiles and eight supersaturation profiles. Each temperature profile varied by 1°C up to 5°C and down to -5°C, while each supersaturation profile was shifted by 2% up to 10% greater than BSPTIC and down 4% from BSPTIC. The results of the simulations will be explored in the next section.

4.3 Results

This section presents the results of the sensitivity experiment described earlier in this chapter. Due to nature of this sensitivity experiment in that numerous simulations were performed, a method for comparison of the simulations needed to be derived that accurately represents the results of each simulation. To compare the simulations within both batches of IN concentrations, a single quantity for each simulation was required. These quantities were then contoured for each batch of IN concentration simulations to identify trends. In order to mask out erroneous numerical instabilities, the following methodology for obtaining a single value for each simulation ensued. First, the time at which the maximum horizontally averaged ice water path occurred was the time used for calculations within the respective simulation. Then for this time, the column average was calculated and used as the final value of the desired quantity. Unless stated otherwise, all figures presented in this section utilized this methodology in displaying the results of the sensitivity experiment and are illustrated in plots of change in temperature profile (ΔT) versus change in supersaturation profile (ΔS) as shown in Figure 4.2. It can be seen from Figure 4.2 that 88 data points (one for each simulation) will be contoured for each batch of IN concentration simulations.

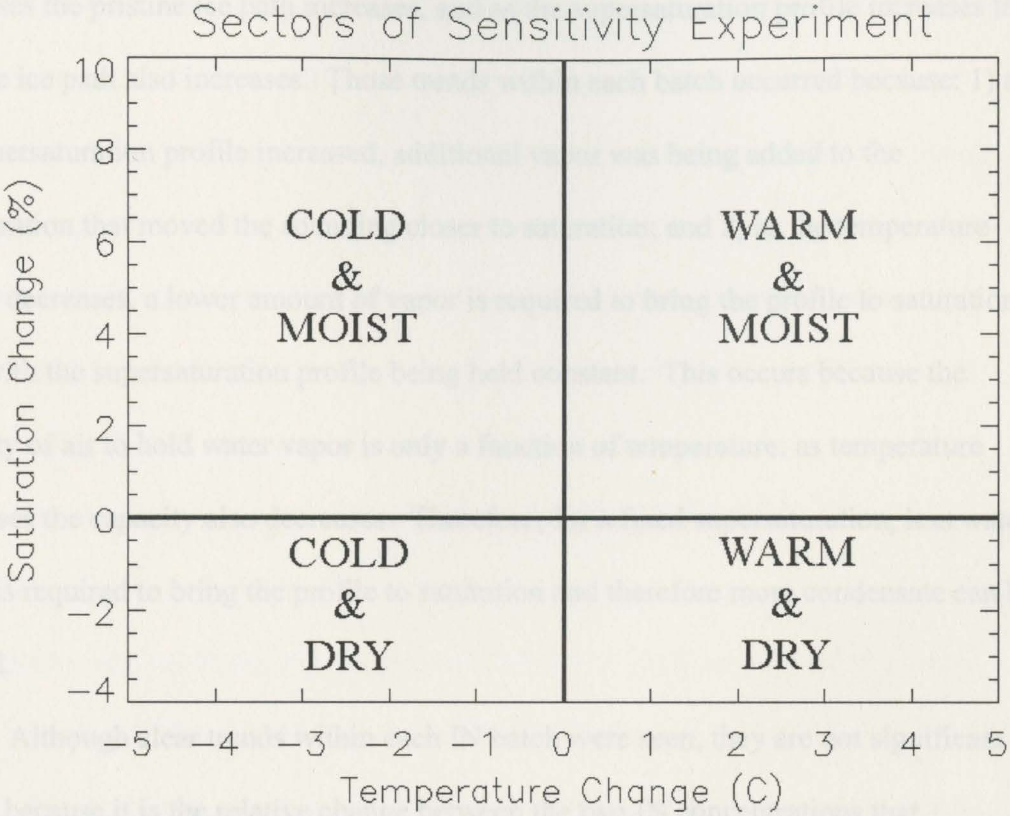

Figure 4.2: Named sectors of the sensitivity experiment relative to the BSPTIC. The horizontal axis is a function of temperature change while the vertical axis is a function of supersaturation change.

4.3.1 Ice Path

The results presented in this section are the maximum ice species' path for each experiment and are not relative to the maximum total ice water path, as described in the beginning of this section.

To begin with, the pristine ice paths are shown in Figure 4.3. The value (0°C,0%) corresponds to the BSPTIC sounding. It can be seen that for both the high IN batch and low IN batch, shown in Figures 4.3 (a) and (b) respectively, as the temperature profile decreases the pristine ice path increases, and as the supersaturation profile increases the pristine ice path also increases. Those trends within each batch occurred because: 1) as the supersaturation profile increased, additional vapor was being added to the initialization that moved the sounding closer to saturation; and 2) as the temperature profile decreases, a lower amount of vapor is required to bring the profile to saturation even with the supersaturation profile being held constant. This occurs because the capacity of air to hold water vapor is only a function of temperature; as temperature decreases the capacity also decreases. Therefore, for a fixed supersaturation, less water vapor is required to bring the profile to saturation and therefore more condensate can be created.

Although clear trends within each IN batch were seen, they are not significant results because it is the relative change between the two IN concentrations that demonstrate the impact of varying IN concentrations. As a result, Figure 4.3 (c) shows the ratio of high to low IN concentrations for each simulation. The regions of low ratios indicate relatively similar pristine ice paths, while the regions of high ratios indicate more dramatic differences. By increasing the IN concentration it is only natural to have an increase in condensate, however the smaller ratios demonstrate a significant increase in pristine ice condensate for the low IN relative to the high IN. The band of lowest ratios, with values less than 5, is stretched from the cold and dry region through BSPTIC and into the warm and moist region. This band provided initial evidence that those simulations could potentially act to remove an increased amount of vapor from the atmosphere and condense it into ice crystals with a lower IN concentration.

Next, the snow paths [Figure 4.4 (a) and (b)] show similar trends to pristine ice of having the maximum paths in the cold and moist sector within each batch of simulations. With respect to the relative change between snow paths, a similar pattern also occurred as compared with pristine ice paths. The same region contained the lowest ratios of snow path, however the minimum ratios concentrated in the warm and moist sector of the experiment showed a slightly stronger signal and had lower values (less than approximately 3) than compared with pristine ice.

The last water category of concern is aggregates. Figures 4.5 (a) and (b) show the aggregate paths for both the high and low IN batch of simulations, respectively. Similar to pristine ice and snow, aggregates also exhibited an overall trend of the maximum values occurring in the cold and moist sector. With respect to the ratio between the high and low IN simulations, as shown in Figure 4.5 (c), the values were significantly higher by almost 2 orders of magnitude larger than compared with pristine ice and snow. This suggests that the low IN simulations had trouble forming aggregates. Although the ratios were fairly large, the relative minimum is in the same location as both pristine ice and snow. This does suggest decent simulation consistency.

Finally, in order to obtain a more global view of all ice species, Figure 4.6 shows the total ice water path (IWP) for all of the simulations. IWP is the summation of pristine ice, snow, and aggregates paths. The values shown in Figures 4.6 (a) and (b) are the maximum IWP for each simulation and the times at which they occur were the profiles used for subsequent figures, as explained earlier in this chapter. Once again, the trend of the maximum values for IWP occurred in the cold and moist sector. The ratio plot [Figure 4.6 (c)] shows the lowest values confined to the warm and moist sector of the figure, however similar to snow, the signature was fairly strong for IWP. The region that consistently showed minimum ratios between the high and low IN simulations was in the warm and moist sector with changes to the BSPTIC temperature profile greater than 2°C and supersaturation changes greater than 2%. Conclusively, this region shows the most significant microphysical change between high and low IN simulations with respect to mass. Next, particle sizes will be explored to determine is the mass differences are a result of larger particle growth.

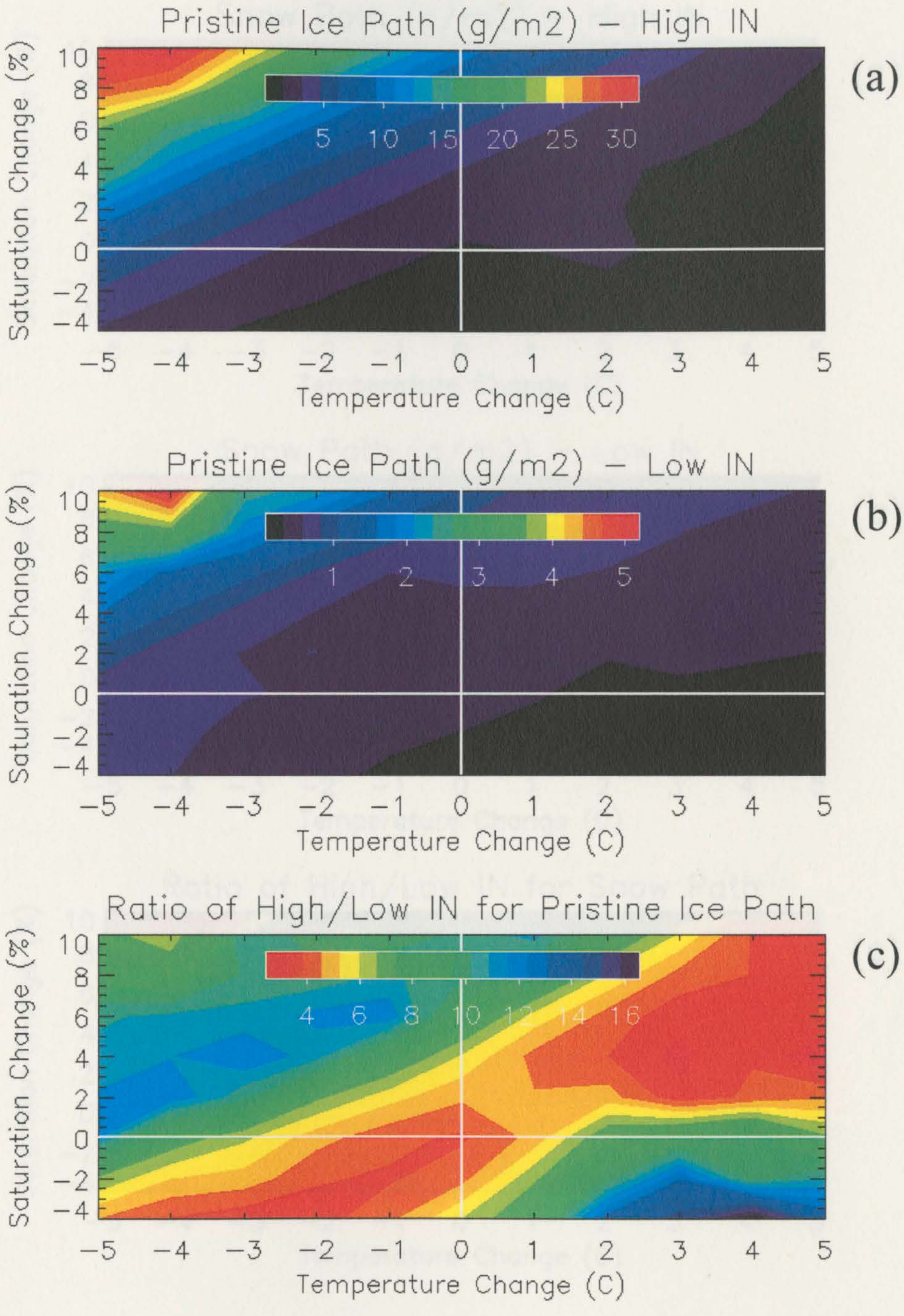

Figure 4.3: Horizontally averaged maximum pristine ice path (g/m^2) for the: (a) high IN concentration simulations, and (b) low IN concentration simulations. (c) Ratio of (a)/(b) values.

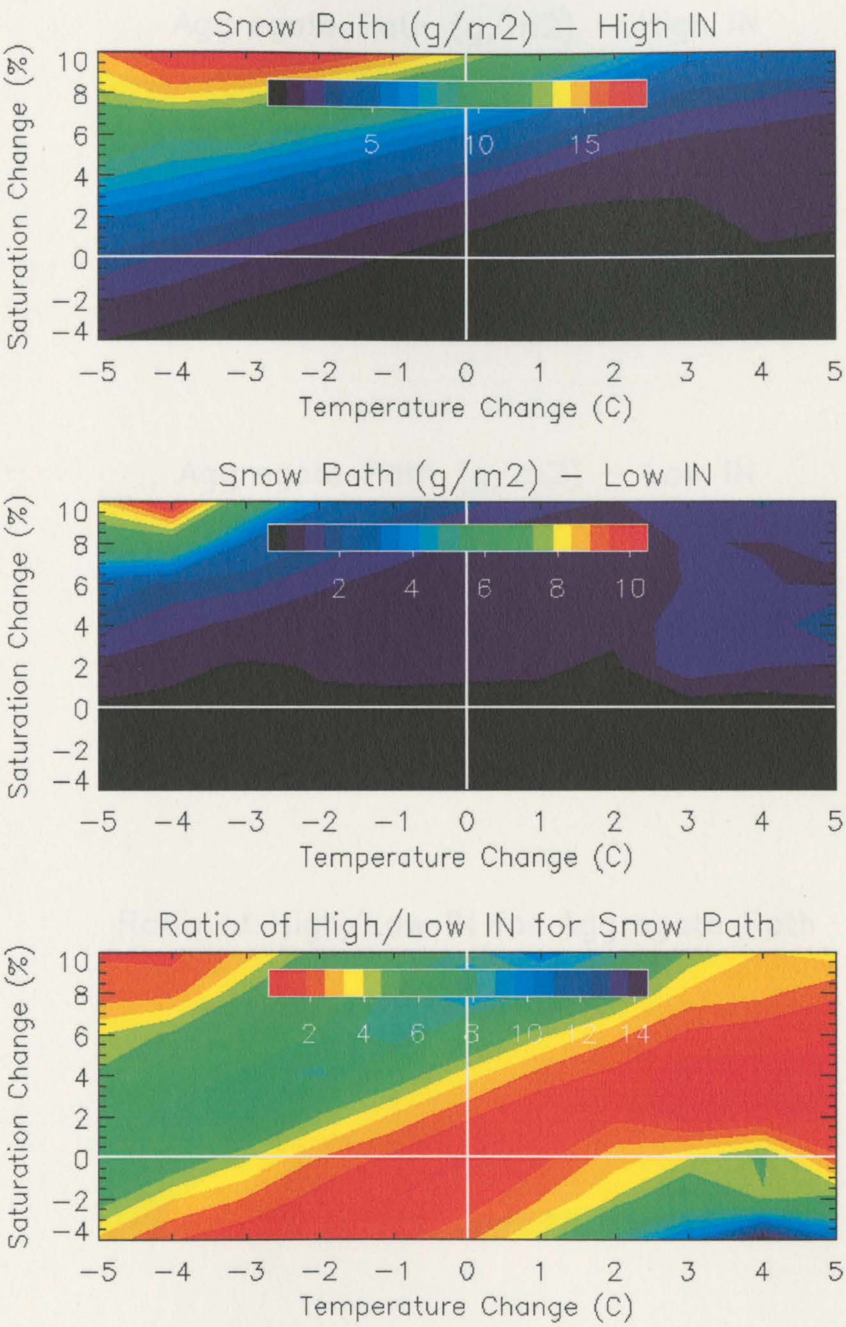

Figure 4.4: Horizontally averaged maximum snow path (g/m^2) for the: (a) high IN concentration simulations, and (b) low IN concentration simulations. (c) Ratio of (a)/(b) values.

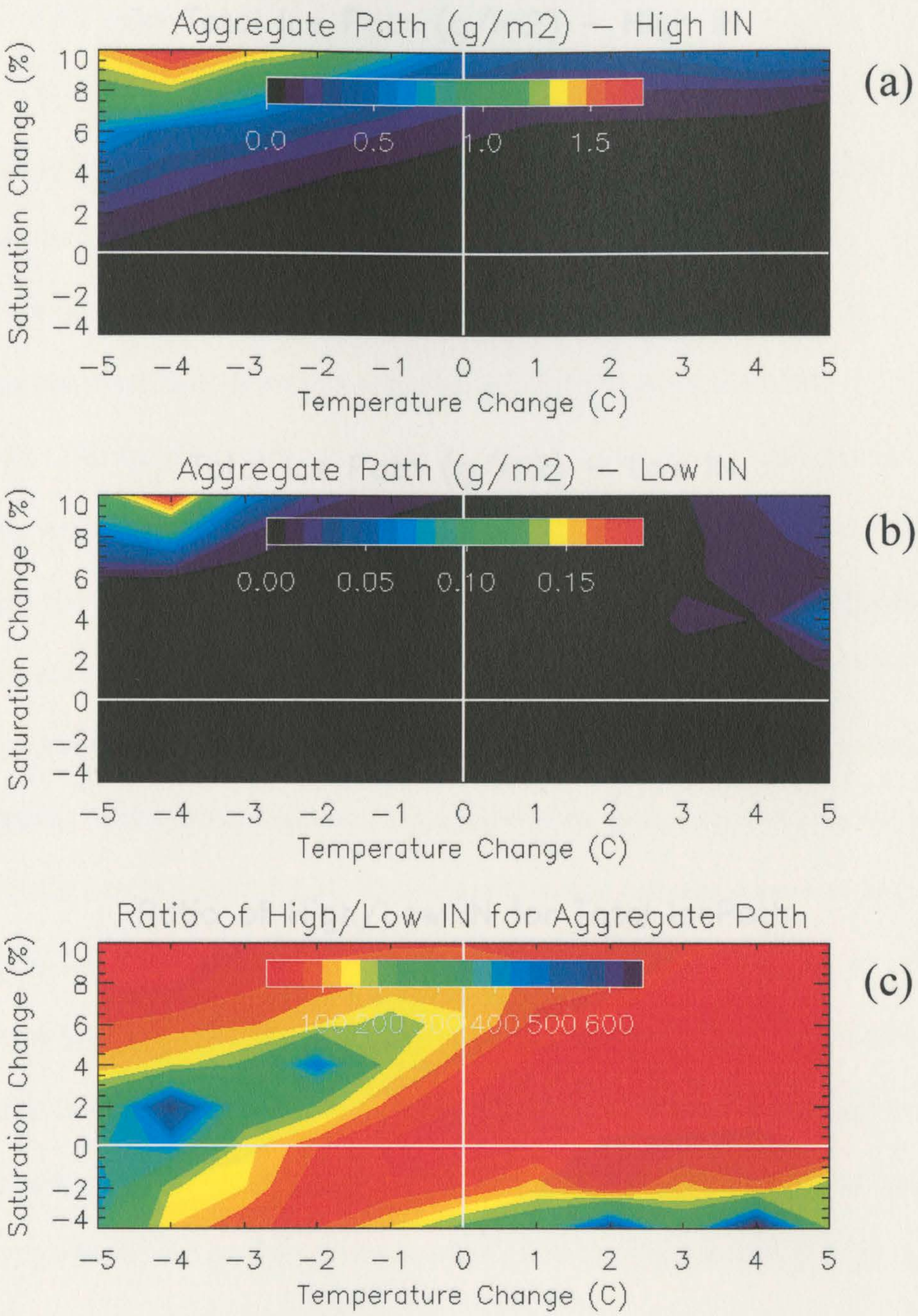

Figure 4.5: Horizontally averaged maximum aggregate path (g/m^2) for the: (a) high IN concentration simulations, and (b) low IN concentration simulations. (c) Ratio of (a)/(b) values.

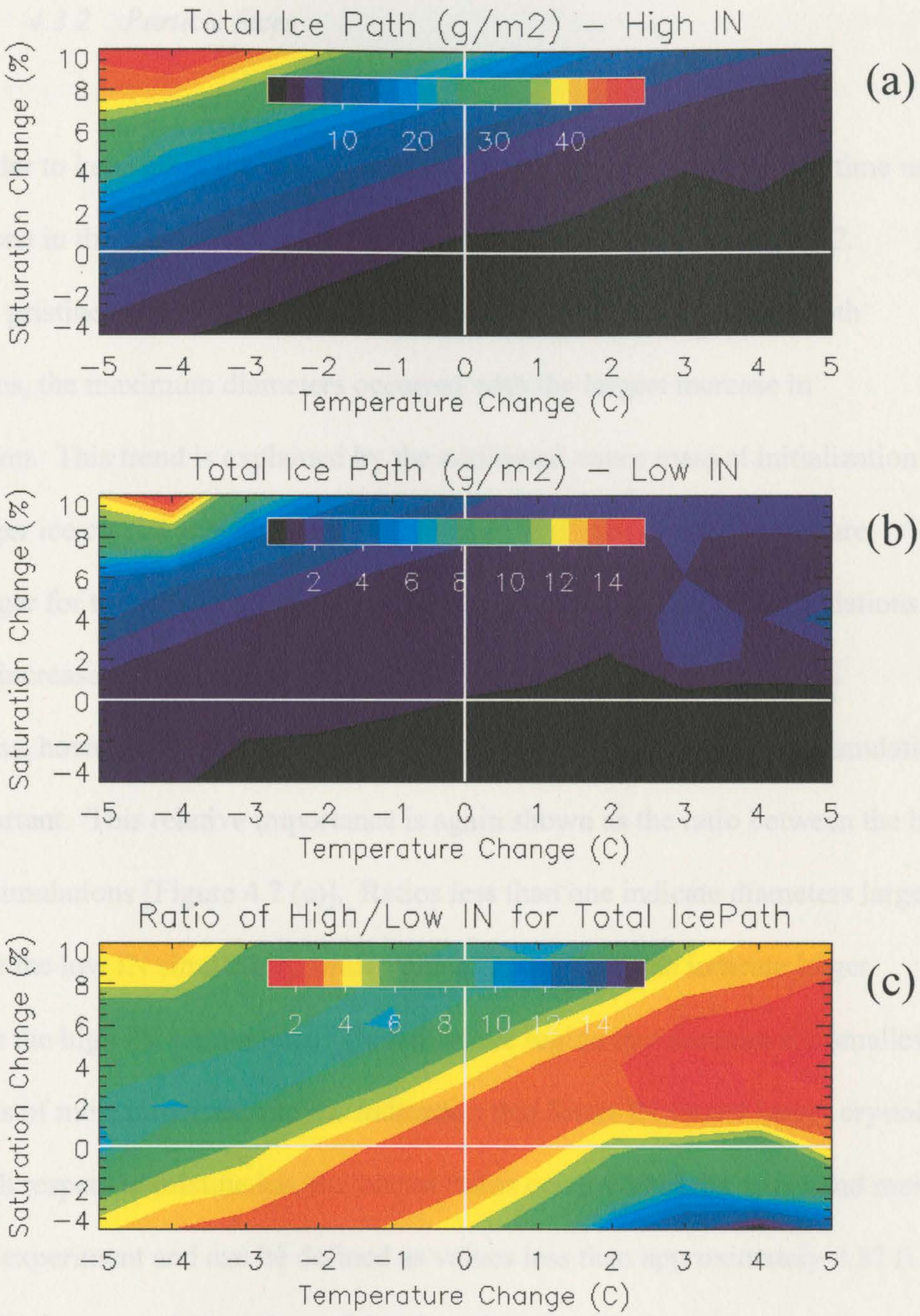

Figure 4.6: Horizontally averaged maximum total ice path (g/m^2) for the: (a) high IN concentration simulations, and (b) low IN concentration simulations. (c) Ratio of (a)/(b) values.

4.3.2 Particle Sizes

In order to keep all of the analysis consistent with each simulation, the time used for calculations in this section is the maximum IWP, as described in section 4.2.

First, pristine ice diameters are shown in Figure 4.7 (a) and (b). For both concentrations, the maximum diameters occurred with the largest increase in supersaturation. This trend is explained by the additional vapor mass at initialization allowing larger ice crystal growth. It is evident that the pristine ice diameters are generally larger for the low IN simulations as compared with the high IN simulations. This overall increase in sizes confirms the theory of larger growth for lower IN concentrations, however the relative difference between the high and low IN simulations is more important. This relative importance is again shown as the ratio between the high and low IN simulations [Figure 4.7 (c)]. Ratios less than one indicate diameters larger diameters for the low IN simulation, while values greater than one indicate larger diameters for the high IN simulations. Therefore, the region that contains the smallest ratio values is of most importance to the indication that fewer IN causes larger crystal growth. With respect to pristine ice, the lowest ratios occur within the warm and moist sector of the experiment and can be defined as values less than approximately 0.87 (i.e. the high IN diameters are 87% or less of the size of the low IN diameters).

Next, Figure 4.8 (a) and (b) shows the mean diameters for snow. Similar to pristine ice, the largest snow diameters existed in the high supersaturation region of the experiment. With respect to the change in snow diameters between the high and low simulations, Figure 4.8 (c) shows the relative change between them. Like pristine ice diameters, the snow diameters were larger for the low IN simulations and the minimum ratios occurred in the warm and moist sector of the experiment. Although the swatch of minimum ratios were shifted slightly towards higher supersaturation profiles, the values were significantly smaller than for pristine ice, with the minimum values generally lower than 0.80 and extending down to below 0.60.

The aggregate sizes for all simulations are shown in Figure 4.9 (a) and (b). Like the other two ice species, aggregate diameter does increase with increasing supersaturation. However unlike pristine ice and snow, the aggregate sizes are generally larger for the high IN simulations, except for two regions: 1) warm and moist sector, and 2) cold and moist sector. These two regions can be seen in Figure 4.9 (c) as the areas with ratio values lower than 1.0 (shown in black). The minimum ratio values in the warm and moist sector coincide with minimum regions of relative change for both snow and pristine ice. However, the region of low ratio values in the cold and moist sector is an anomalous group of experiments relative to the other ice species' particle sizes. Therefore, the warm and moist experiments with minimum relative change between the high and low IN simulations provided the strongest signal in the reproduction of TIC's because of the evident overlapping in experiments with both pristine ice and snow. As confirmation, a collective look at the ice diameters relative to mass is needed.

In order to quantitatively compare all ice species' diameters, Figure 4.10 illustrates the mass weighted ice diameter for all ice phases. By weighting the diameters of each species with their respective masses, a single diameter can be derived for the total distribution of ice species that provides an excellent means for comparison between the high and low IN simulations. It was computed as the sum of each ice species' effective diameter multiplied by their respective mass and then normalized by the total mass. Figure 4.10 (a) and (b) show the mass weighted diameters for both batches of simulations. It can be seen that overall, the diameters were larger for the low IN simulations as compared with the high IN simulations. To quantitatively measure that, Figure 4.10 (c) shows the ratio between the simulations. As seen with each ice species, the mass weighted diameter showed a region of minimum values located in the warm and moist sector of the experiment. More specifically, the region is bounded by the profiles that have a temperature increase greater than 2°C and supersaturation increase between 0% and 6%. This region demonstrates that the high IN simulations had mass weighted diameters that were generally 60% of the size of the low IN simulations. The following section will briefly explore ice number concentrations to check the consistency with previously examined masses and diameters.

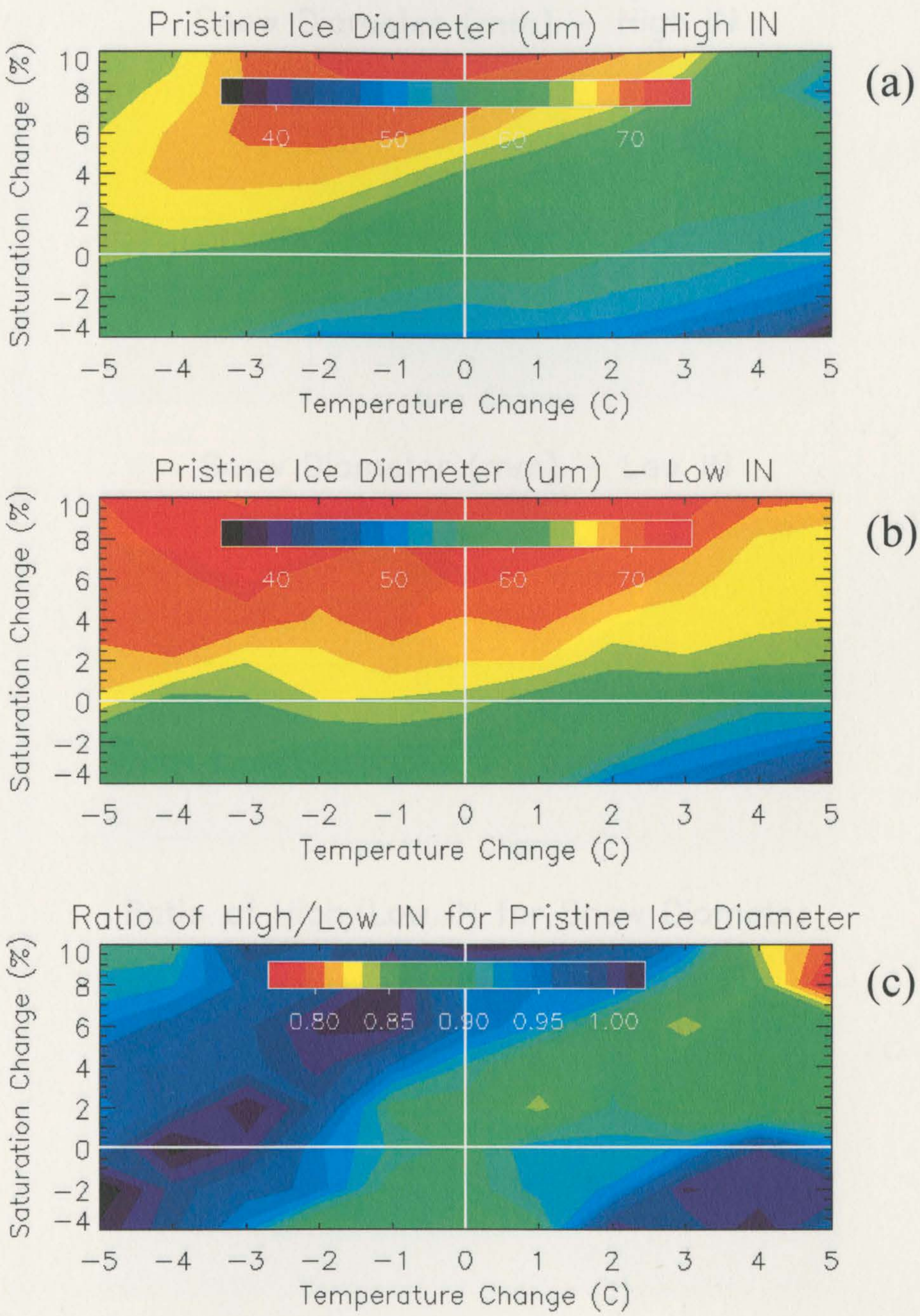

Figure 4.7: Vertical average of horizontally averaged pristine ice diameters (μm) at the time of maximum IWP for the: (a) high IN concentration simulations, and (b) low IN concentration simulations. (c) Ratio of (a)/(b) values.

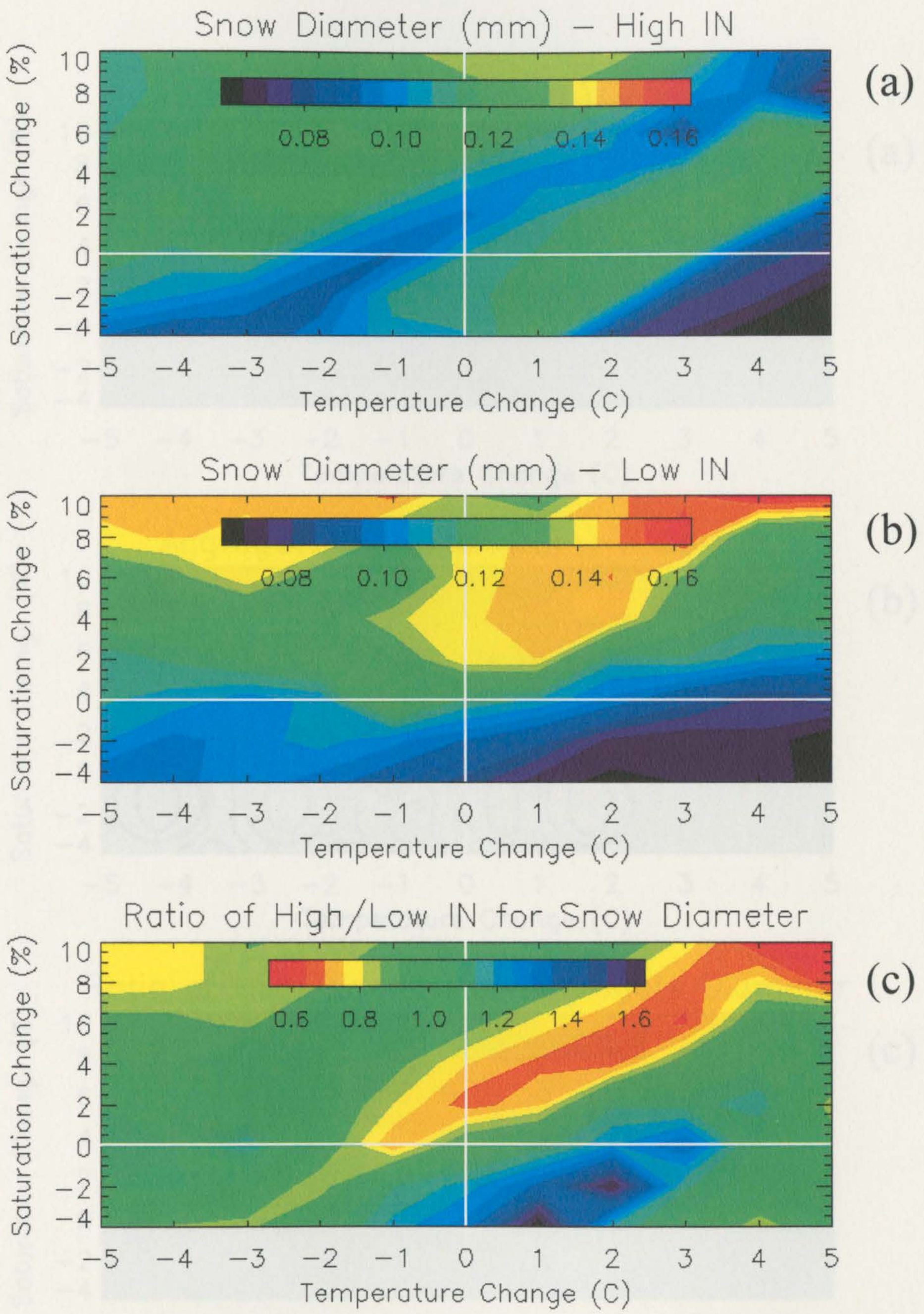

Figure 4.8: Vertical average of horizontally averaged snow diameters (mm) at the time of maximum IWP for the: (a) high IN concentration simulations, and (b) low IN concentration simulations. (c) Ratio of (a)/(b) values.

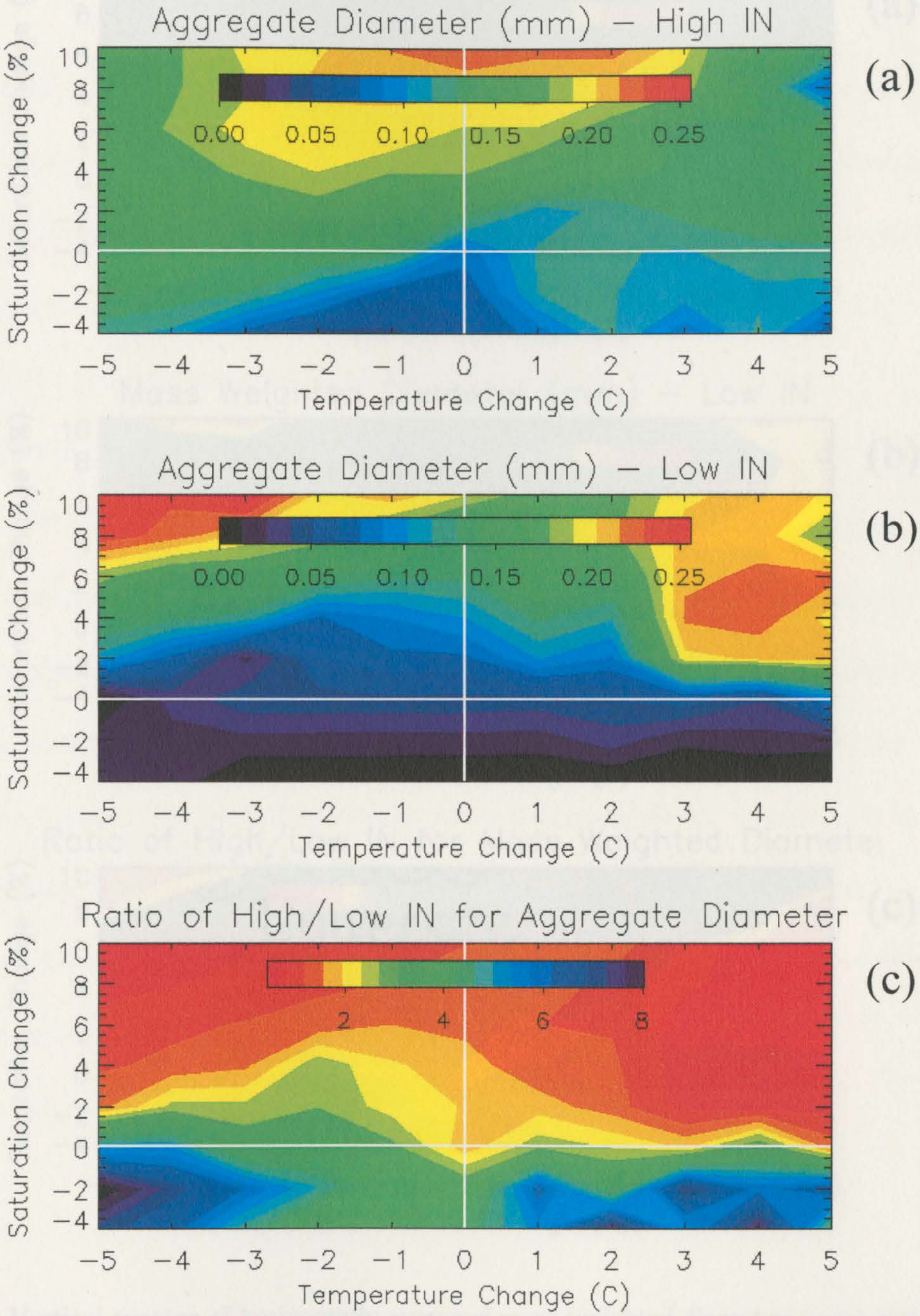

Figure 4.9: Vertical average of horizontally averaged aggregate diameters (mm) at the time of maximum IWP for the: (a) high IN concentration simulations, and (b) low IN concentration simulations. (c) Ratio of (a)/(b) values.

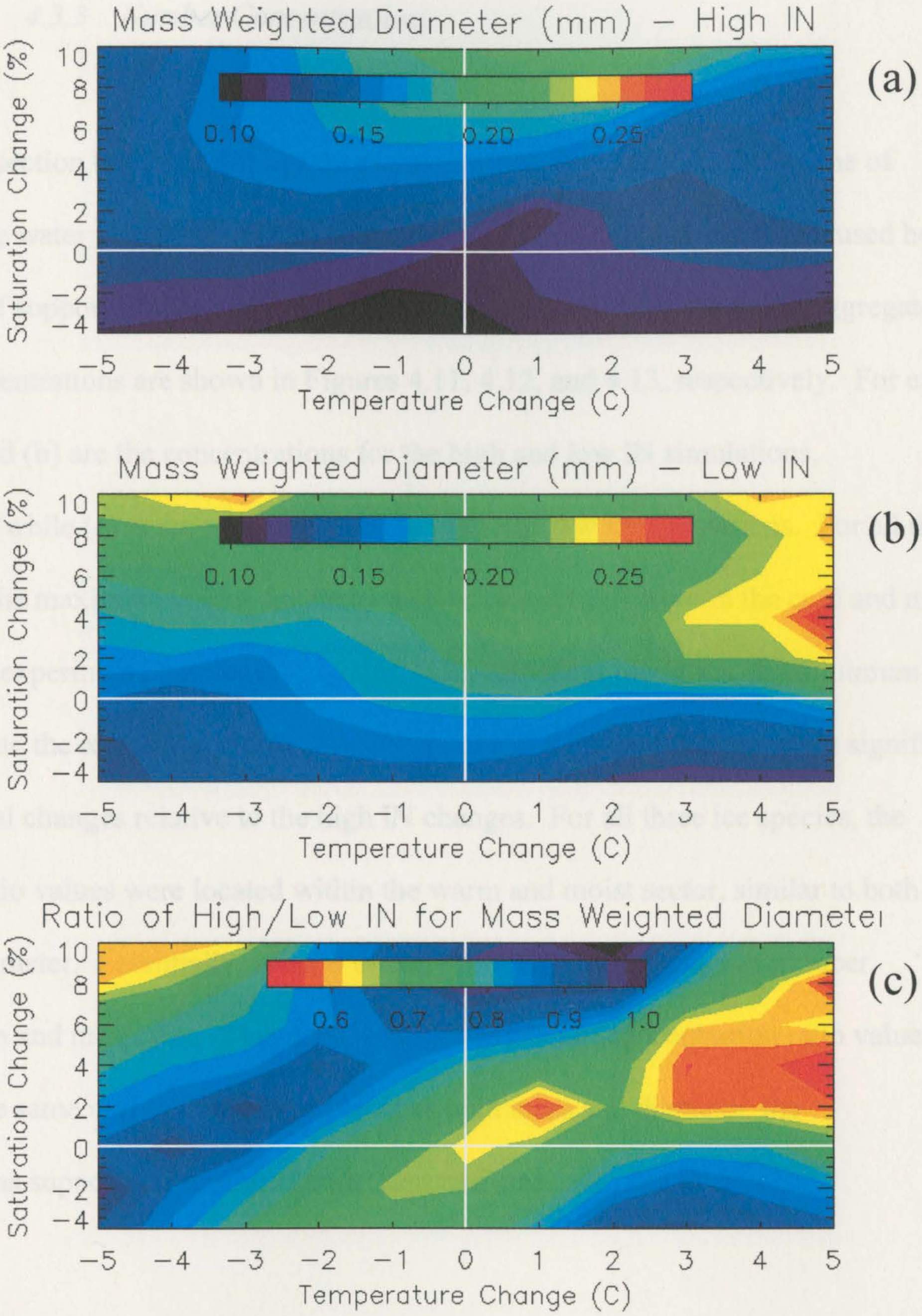

Figure 4.10: Vertical average of horizontally averaged mass-weighted diameters (mm) at the time of maximum IWP for the: (a) high IN concentration simulations, and (b) low IN concentration simulations. (c) Ratio of (a)/(b) values.

4.3.3 Number Concentrations

This section briefly examines the mean number concentration at the time of maximum ice water path for each ice species, as number concentration is only used here as a means of support for ice mass and particle sizes. Pristine ice, snow and aggregate number concentrations are shown in Figures 4.11, 4.12, and 4.13, respectively. For each figure, (a) and (b) are the concentrations for the high and low IN simulations, respectively, while (c) is the ratio between the high and low IN simulations. For all three ice species, the maximum values for each batch of simulations were in the cold and moist sector of the experiment, similar to ice path. With respect to the ratios, the minimum values indicate the regions where the low IN simulations demonstrate the most significant microphysical changes relative to the high IN changes. For all three ice species, the minimum ratio values were located within the warm and moist sector, similar to both mass and diameter. Essentially, mass is directly related to the product of number concentration and mean size. Therefore, with the minimum concentration ratio values located in the same region of the experiment as both mass and diameter, the concentrations support the results of both mass and size.

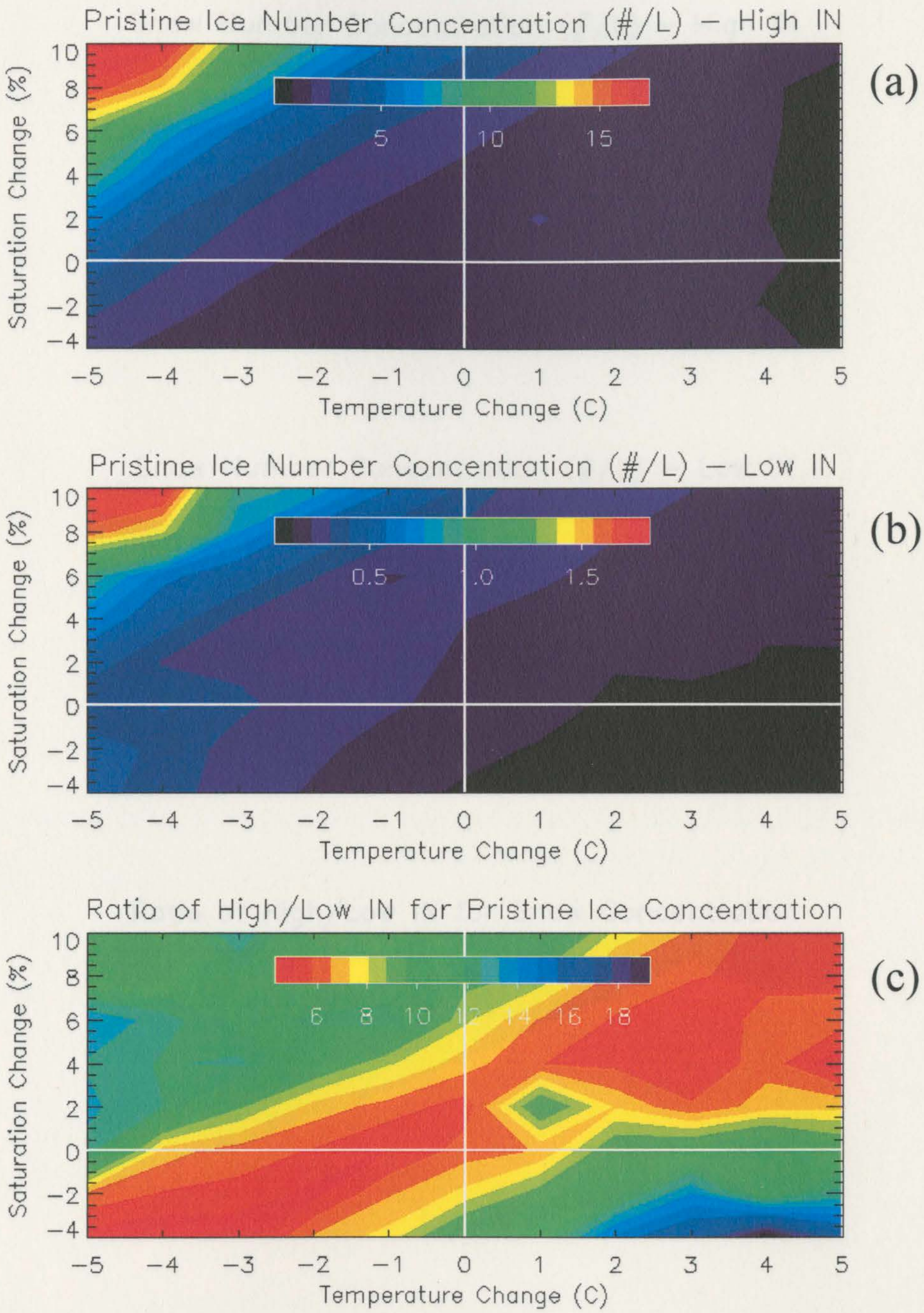

Figure 4.11: Vertical average of horizontally averaged pristine ice concentrations (L^{-1}) at the time of maximum IWP for the: (a) high IN concentration simulations, and (b) low IN concentration simulations. (c) Ratio of (a)/(b) values.

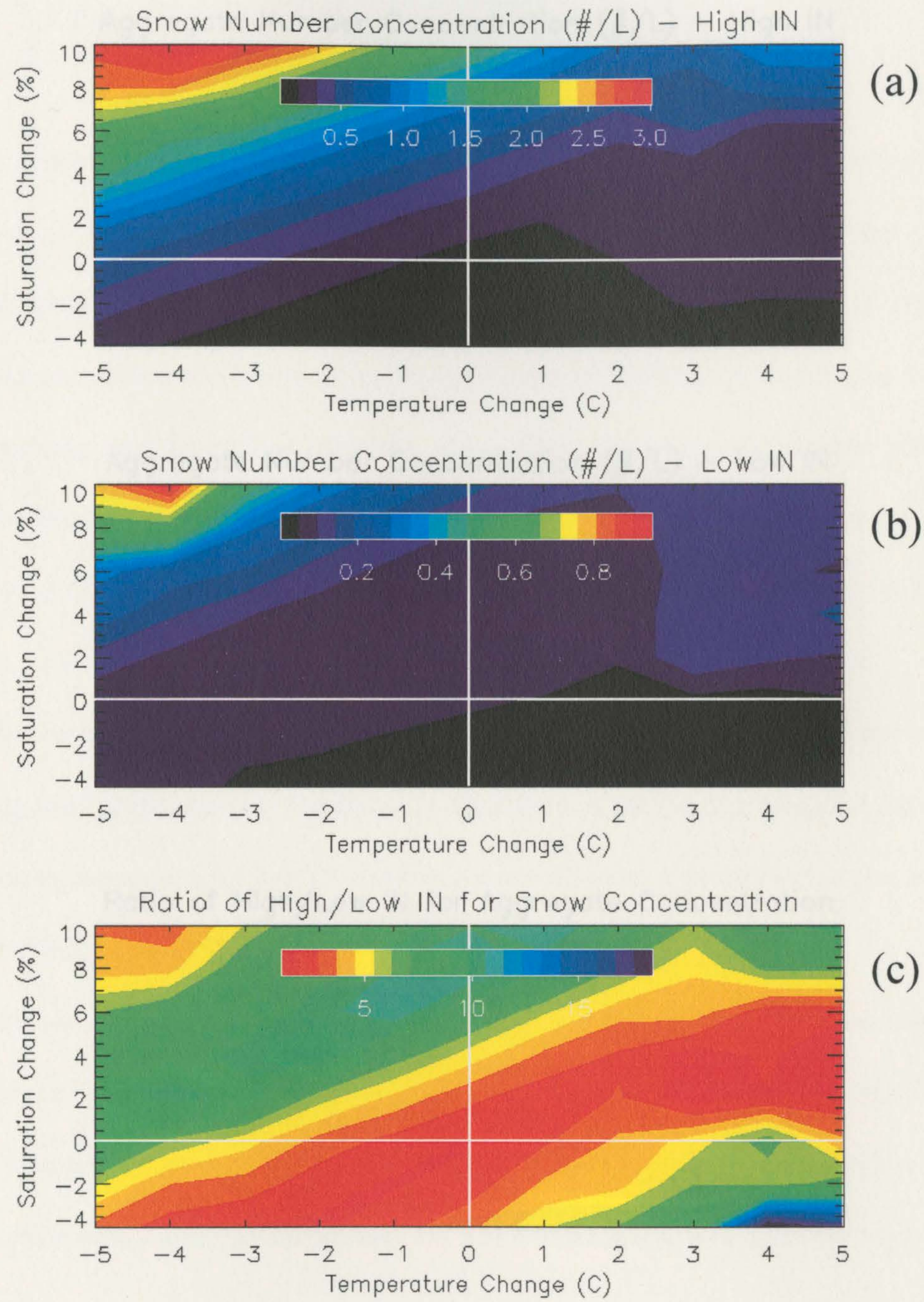

Figure 4.12: Vertical average of horizontally averaged snow concentrations (L^{-1}) at the time of maximum IWP for the: (a) high IN concentration simulations, and (b) low IN concentration simulations. (c) Ratio of (a)/(b) values.

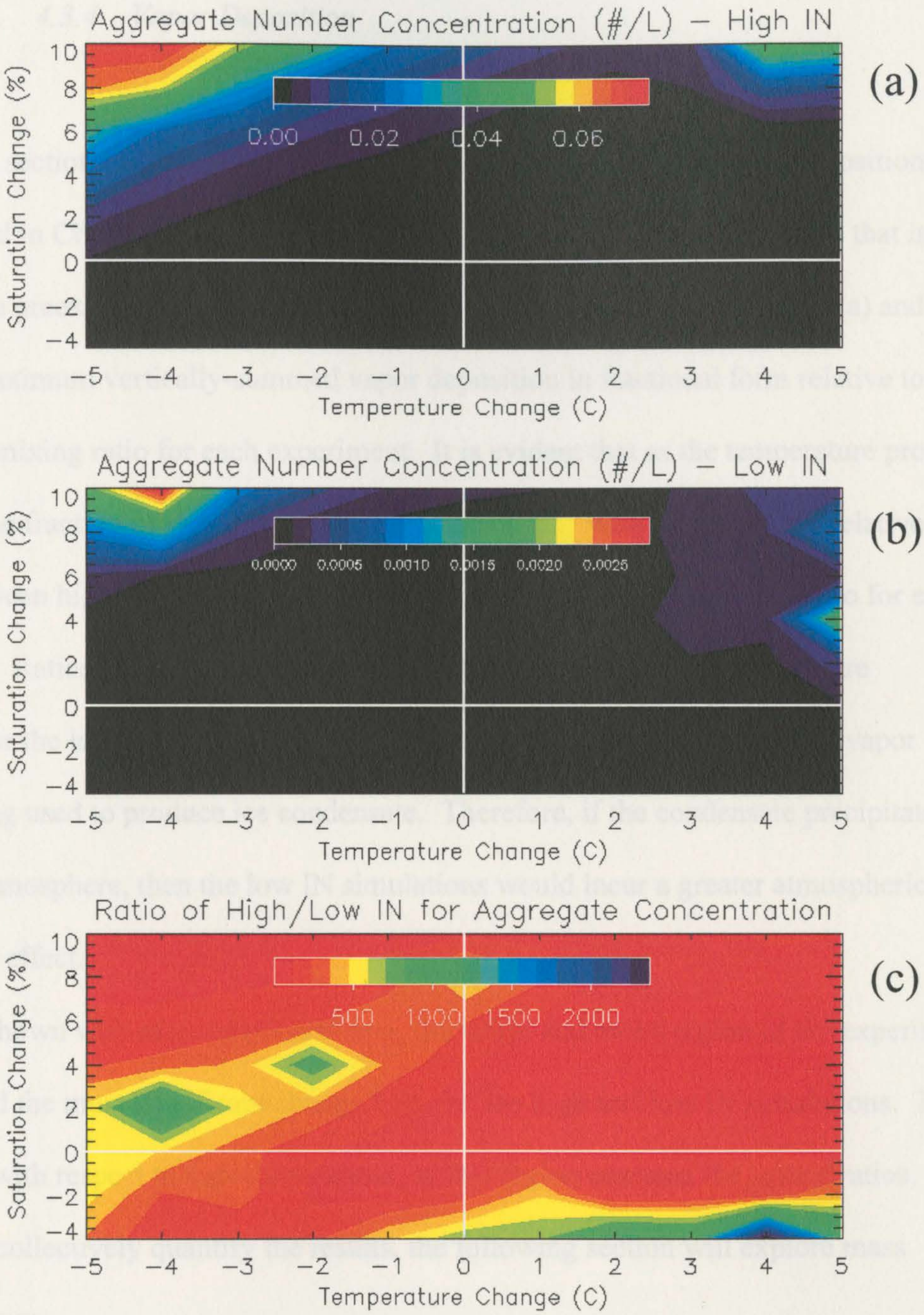

Figure 4.13: Vertical average of horizontally averaged aggregate concentrations (L^{-1}) at the time of maximum IWP for the: (a) high IN concentration simulations, and (b) low IN concentration simulations. (c) Ratio of (a)/(b) values.

4.3.4 Vapor Deposition

This section briefly examines the RAMS internal variable of vapor deposition. As explained in Chapter 3, vapor deposition is the amount of water vapor mass that is deposited on preexisting ice crystals (i.e. pristine ice and snow). Figures 4.14 (a) and (b) show the maximum vertically-summed vapor deposition in fractional form relative to pristine ice mixing ratio for each experiment. It is evident that as the temperature profile increases, the fraction of vapor deposition also increases. With respect to the relative change between high and low IN concentrations, Figure 4.14 (c) shows the ratio for each experiment. Ratios less than 1.0 indicate that vapor deposition is relatively more important for the low IN simulations, which means that a higher percentage of vapor mass is being used to produce ice condensate. Therefore, if the condensate precipitates out of the atmosphere, then the low IN simulations would incur a greater atmospheric dehydration effect.

As shown with aforementioned data, the warm and moist region of the experiment has provided the most significant change between the high and low IN simulations. This is also true with respect to vapor deposition, as this region contains the lowest ratios. In an effort to collectively quantify the results, the following section will explore mass depletion times.

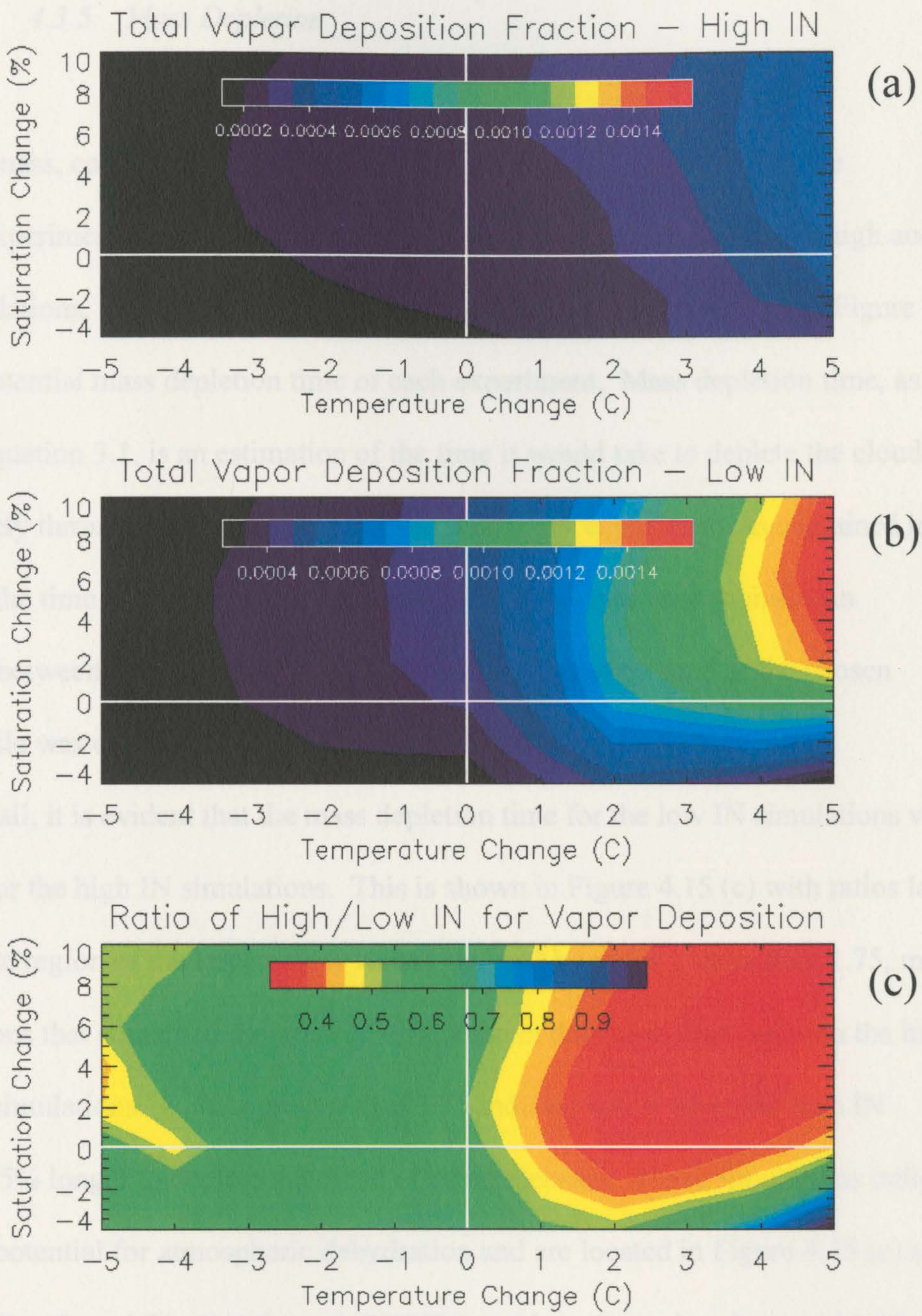

Figure 4.14: Maximum vertically summed vapor deposition divided by total pristine ice mixing ratio for: (a) high IN concentration simulations, and (b) low IN concentration simulations. (c) Ratio of (a)/(b) values.

4.3.5 Mass Depletion

The mass, concentration, and size data all pointed to a region within the sensitivity experiment that demonstrated appreciable differences between the high and low IN simulations. In an effort to summarize all of the aforementioned data, Figure 4.15 shows the potential mass depletion time of each experiment. Mass depletion time, as shown by Equation 3.1, is an estimation of the time it would take to deplete the cloud of its mass purely through sedimentation. For the sensitivity experiment, as explained in section 4.2, the time at which the maximum IWP occurred was used to maintain consistency between simulations and an average mass depletion time of the chosen vertical profile was calculated for each experiment [Figure 4.15 (a) and (b)].

Overall, it is evident that the mass depletion time for the low IN simulations were lower than for the high IN simulations. This is shown in Figure 4.15 (c) with ratios larger than 1.0. The region of the largest ratio values, defined by ratios greater than 1.75, mark the simulations that contained the greatest difference in depletion time between the high and low IN simulations. Values greater than 1.75 indicate that it takes the high IN simulation 75% longer to deplete the cloud of its condensate. These simulations indicate the greatest potential for atmospheric dehydration and are located in Figure 4.15 (c) as a swath extending from [-2°,-4%] through BSPTIC and into the region that was highlighted by the mass, concentration, and diameter data. The following section will analyze and compare the data presented in section 4.3.

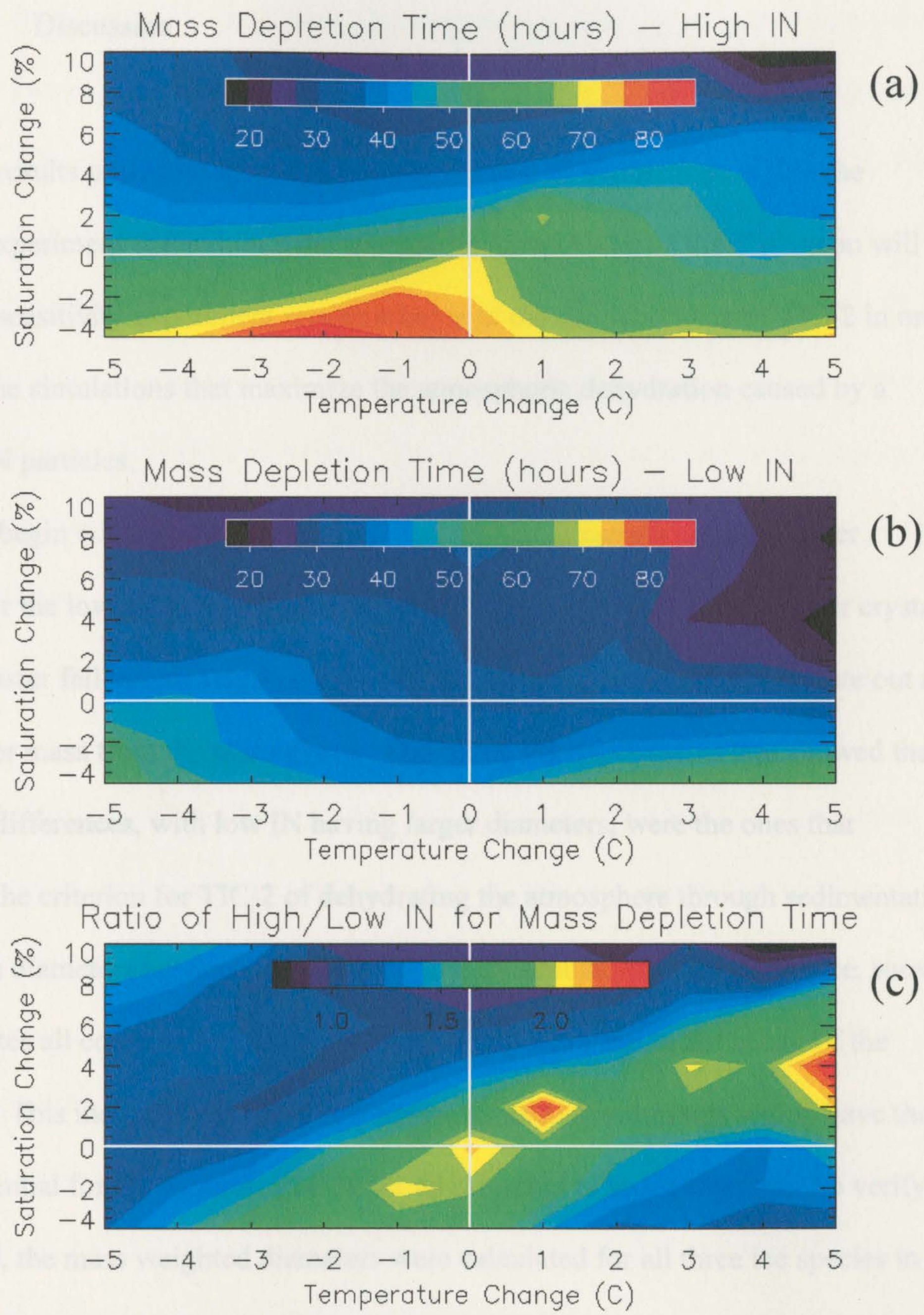

Figure 4.15: Horizontally averaged mass depletion time (s) at the time of maximum IWP for the: (a) high IN concentration simulations, and (b) low IN concentration simulations. (c) Ratio of (a)/(b) values.

4.4 Discussion

The results presented above all point to a group of simulations within the sensitivity experiment that exhibits the characteristics of TIC-2. This discussion will analyze the sensitivity experiment results relative to the characteristics of TIC-2 in order to identify the simulations that maximize the atmospheric dehydration caused by a coating of IN particles.

To begin with, pristine ice and snow diameters generally showed larger diameters for the low IN simulations relative to the high IN simulations. Larger crystal sizes have faster fall speeds within the clouds and are more likely to sedimentate out and remove water mass from the atmosphere. Therefore, the experiments that showed the largest size differences, with low IN having larger diameters, were the ones that maximized the criterion for TIC-2 of dehydrating the atmosphere through sedimentation. The ratios in diameters between the high and low IN simulations for pristine ice, snow, and aggregates all contained a minimum value in the warm and moist sector of the experiment. This indicated that the experiments contained within this region have the greatest potential for the formation of TIC-2 with respect to sedimentation. To verify those results, the mass weighted diameters were calculated for all three ice species in order to more effectively view the entire ice crystal distribution. Similar to the individual ice species' diameters, the mass weighted diameters showed the same experiments to have maximized the TIC-2 characteristics.

Next, to see if the warm and moist experiments were actually producing more relative condensate for the low IN simulations and not just a few large crystals, mass and number concentrations were examined. Once again, it is the relative importance between the high and low IN simulations for mass and number concentrations that is significant. The relative difference between high and low IN simulations for both mass and number concentration for all three ice species showed similar regions of minimum values within the warm and moist sector of the experiment, which were also the same experiments for ice diameters. Additionally, vapor deposition was examined with its relative importance between the high and low IN simulations. The warm and moist sector of the experiment, similar to the abovementioned results, showed larger vapor deposition fractions for the low IN simulations as compared with the high IN simulations. These results further indicate the effective dehydration of vapor mass from the atmosphere and onto ice condensate.

In an effort to confirm those results, mass depletion time was calculated as a method to estimate how potentially effective each experiment was in removing mass from the atmosphere. Short mass depletion times indicated that the experiments were potentially more effective in removing water mass from the atmosphere. Therefore, the largest ratios between the high and low IN simulations indicated that the respective experiments represented the most likely candidates for TIC-2. From the mass depletion time ratios, it can be seen that the same group of experiments described above contained the largest ratio values. More specifically, the cluster of experiments showing the strongest similarity to the characteristics of TIC-2 within the warm and moist sector can be bounded by a general region in which the temperature profile modifications were greater than 2°C and supersaturation profile changes were greater than 0% and less than or equal to 6%. For the low IN simulations of these experiments, they contained a relatively large amount of mass consisting of large particle sizes that could more effectively sedimentate out of the atmosphere, thus causing dehydration. Conclusively, of the 88 combinations of initial conditions tested in this sensitivity experiment, these 9 experiments displayed the most similarity to PTIC-2.

The following chapter will discuss and compare the overall results of both the PEARL case study and the sensitivity experiment.

CHAPTER 5

CONCLUSIONS AND SUGGESTIONS FOR FUTURE RESEARCH

5.1 Summary and Conclusions

The purpose of this study was to simulate an Arctic wintertime cloud signature (TIC-2) observed by CloudSat and CALIPSO. The signature is hypothesized to form due to an acid coating on IN particles that render them inactive, therefore reducing the number of potential ice crystals and causing larger crystal growth that results in increased sedimentation and an atmospheric dehydration effect. The results of the case study (PTIC) simulations did not provide concrete evidence that supports this hypothesis. The inconclusive results could partly be attributed to the uncertainties that exist in radiosonde measurements; especially while Arctic winter is extremely sensitive to changes in atmospheric water vapor. For this reason, a sensitivity experiment was conducted with a goal of identifying the initial environmental conditions that maximize the support of the hypothesis. This section summarizes the most significant results of both the case study simulations and the sensitivity experiment.

The PEARL case study simulations (PTIC) showed inconclusive support of the hypothesis. Temporally, PTIC had two separate cloud events, Area 1 and Area 2, which were analyzed. Area 1 demonstrated more significant changes microphysically between

PTIC-h and PTIC-l [high and low IN simulations, respectively] as compared with Area 2 and will therefore be summarized further.

The pristine ice diameters showed significant change with PTIC-l having nearly twice as large diameters versus PTIC-h, while the pristine ice mass and number concentrations both illustrated a linear increase of 20 times larger for PTC-h. However, the linear increase for both pristine ice mass and number concentration was mainly attributed to the similar increase in IN concentrations [shown by Equation 2.6 (N_{IN})]. Snow was produced by PTIC-h, whereas it did not occur in PTIC-l. Although this was due to sedimentation into decreased supersaturation in the lower portion of the cloud for PTIC-l, it illustrated a lack of mass removal for PTIC-l. Snow is generally more effective at removing mass than pristine ice due to its larger fall speed, however a mass depletion time was calculated as a means of quantifying the dehydration potential through sedimentation. The depletion times were generally smaller for PTIC-l as compared with PTIC-h, which meant that the dehydration potential for PTIC-l was stronger. The depletion times however, were not significantly different. As a result of some contradicting results from the PTIC simulations, the sensitivity experiment was performed.

The sensitivity experiment used the PEARL sounding within Area 1 of PTIC as the benchmark for adjusting the temperature and supersaturation profiles. The results of the experiment outlined a distinct group of experiments that maximized the hypothesis. The ratios between the high and low IN simulations for all three ice species (pristine ice, snow, and aggregates) of mean mass diameters, ice paths, ice number concentrations and vapor deposition all showed the same experiments to have the smallest values. The smaller ratios indicated that the low IN simulations had: 1) larger diameters, 2) less difference in masses and concentrations, especially relative to the large difference in IN concentrations, and 3) a relative increase of vapor mass being extracted from the atmosphere and deposited on ice crystals . These attributes indicated that the collection of simulations in the moist and warm sector of the experiment showed larger ice crystals with relatively high amounts of mass for the low IN simulations, which could then sedimentate and act to dehydrate the atmosphere. To confirm the results, mass depletion times were calculated and they showed that the same simulations exhibited significantly smaller depletion times for the low IN simulations, which indicated a higher potential for those simulations to sedimentate mass out and dehydrate the atmosphere.

Overall, the case study simulations were inconclusive in support of the hypothesis. However, the sensitivity experiment that was conducted to discover the environmental conditions that would support the hypothesis showed a group of simulations with a strong signature. The experiments initialized with a warmer and more saturated initial environmental sounding demonstrated that with lower IN concentrations, larger crystals could form and precipitate out, thus dehydrating the Arctic atmosphere. While the sensitivity experiment provides insight as to which environmental conditions maximize TIC-2, a case study simulation with observations that supports the hypothesis is desired. Possible directions for this future work are submitted for consideration in the next sub-section.

5.2 Future Work

Despite the lack of conclusive results for the PEARL case study, the signatures seen by CloudSat and CALIPSO show cloud formations that resemble sedimentation fall streaks of thin ice clouds. The results from the sensitivity experiment provided insight as to which environmental conditions would create microphysical conditions to reproduce these satellite observations. This section provides possible directions for future work and simulations of thin ice clouds.

While the PTIC case study simulations did not provide concrete evidence to support the hypothesis, the sensitivity experiment gave insight as to which environmental conditions produced the most prominent characteristics of TIC's. The sensitivity experiments used only an initial sounding for the duration of the simulations, while the case study simulations were nudged every timestep with observations taken every 12 hours. Future simulations of the PEARL case study, with a similar framework as PTIC, could employ nudging with modifications to each observation profile based on the results of the sensitivity experiment (i.e. increasing the temperature and supersaturation profiles) instead of simply initializing the simulations with the modified sounding.

Within the sensitivity experiment, additional analysis could be made that show the most promise (Warm and Moist initial conditions relative to the benchmark sounding) for the production of TIC-2's and atmospheric dehydration. The additional analysis would consist of quantifying the level of water vapor dehydration due to sedimentation of ice crystals from the Arctic atmosphere. By calculating temporal variations in total water vapor path within these experiments, it would allow for a more representative measure of the climatological impacts of atmospheric dehydration.

With respect to the model microphysics, changes could be made to more accurately simulate the effect of coating IN particles. Blanchet and Girard (2001) show that when air-cooling is slow and vapor pressure is in near equilibrium with aerosol surfaces, either homogeneous or heterogeneous nucleation selectively favors the ice nucleation of coated IN particles at the large end of the particle size spectrum. Since RAMS microphysics used in this study is based on lognormal distributions of particles, this hypothesis could not be tested. Therefore, future simulations could use explicit microphysics with emphasis on the larger end of the particle size spectrum.

Finally, although PTIC was a classic example of TIC-2, the observations taken by radiosondes that were used for nudging likely contained uncertainties, as the clouds are extremely sensitive to even small changes in water vapor. In this study it was corrected by adding additional mass to the vapor profile to account for the condensate, however future work could involve additional case studies in which more observations are available. For example, environmental profiles measured by instruments other than radiosondes along with measurements of IN concentrations would be desired.

REFERENCE LIST

Adams, J. M., N. A. Bond, and J. E. Overland, 2000: Regional variability of the Arctic heat budget in fall and winter. *J Climate,* **13,** 3500-3510.

Albrecht, B. A., 1989: Aerosols, cloud microphysics, and fractional cloudiness. *Science,* **245,** 1227-1230.

Beryland, T. G., and L. A. Strokina, 1980: *Global Distribution of Total Cloud Amount.* Gidrometeoizdata, Leningrad (translated by S. Warren, University of Washington).

Bigg, E. K., 1980: Comparison of aerosol at four baseline atmospheric monitoring stations. *J. Appl. Meteor.,* **19,** 521-533.

Borys, R. D., 1989: Studies of ice nucleation by Arctic aerosols on AGASP-II. *J. Atmos. Chem.,* **9,** 169-185.

Carrio, G. G., H. Jiang, and W. R. Cotton, 2005: Impact of aerosol intrusions on the Arctic boundary layer clouds. Part I: 4 May 1998 case. *J. Atmos. Sci.*, **62,** 3082-3093.

Christensen, J. H., 1997: The Danish Eulerian hemisphere model – A three-dimensional air pollution model used for the Arctic. *Atmos. Environ.,* **31,** 4169-4191.

Cotton, W. R., and Coauthors, 2003: RAMS 2001: Current status and future directions. *Meteo and Atmos. Phys.,* **82,** 5-29.

Curry, J. A., D. Randall, W. B. Rossoe, and J. L. Schramm, 1996: Overview of Arctic cloud and radiation characteristics. *J. Climate,* **9,** 1731-1764.

DeMott, P. J., M. P. Meyers, and W. R. Cotton, 1994: Parameterization and impact of ice initiation processes relevant to numerical model simulations of cirrus clouds. *J. Atmos. Sci.*, **53,** 77-90

Flatau, P. J., G. J. Tripoli, J. Verlinde, and W. R. Cotton, 1989: *The CSU-RAMS Cloud Microphysical Module: General Theory and Code Documentation.* Colorado State University, Department of Atmospheric Science, Fort Collins, CO 80523. Atmos. Sci. Pap., 451, 88 pp.

Girard, E., and J.-P. Blanchet, 2001: Microphysical parameterization of Arctic diamond dust, ice fog, and thin stratus for climate models. *J Atmos. Sci.,* **58,** 1181-1198.

Girard, E. and J.-P. Blanchet, 2001: Simulation of Arctic diamond dust, ice fog, and thin stratus using an explicit aerosol-cloud-radiation model. *J. Atmos. Sci.,* **58,** 1199-1221.

Gorshkov, S. G., 1983: *World Ocean Atlas.* Vol. 3, *The Arctic Ocean.* Permagon Press.

Grenier, P., J.-P. Blanchet, and R. Munoz-Alpizar, 2009: Study of polar thin ice clouds and aerosols seen by CloudSat and CALIPSO during midwinter 2007. *J. Geophys. Res.,* **114,** D09201, doi:10.1029/2008JD010927

Hahn, C. J., S. G. Warren, and J. London, 1995: The effect of moonlight on observation of cloud cover at night, and application to cloud climatology. *J. Clim.,* **8,** 1429-1446.

Harrington, J. Y., 1997: *The effects of radiative and microphysical processes on simulated warm and transitional season Arctic stratus.* PhD Diss., Atmospheric Science Paper No 637, Colorado State University, Department of Atmospheric Science, Fort Collins, CO 80503, 289 pp.

Harrington, J. Y., M. P. Meyers, R. L. Walko, and W. R. Cotton, 1995: Parameterization of ice crystal conversion processes due to vapor deposition for mesoscale models using double-moment basis functions. Part I: Basic formulation and parcel model results. *J. Atmos. Sci.,* **55,** 45-75.

Harrington, J. Y., T. Reisin, W. R. Cotton, and S. M. Kreidenweis, 1999: Cloud resolving simulations of Arctic stratus. Part II: Transition-season clouds. *J. Atmos. Sci,* **57,** 766-785.

Huschke, R. E., 1969: *Arctic cloud statistics from "air-calibrated" surface weather observations.* The Rand Corporation, RM-6173-PR, 79 pp.

Intrieri, J. M., M. D. Shupe, T. Uttal, and B. J. McCarty, 2002: An annual cycle of Arctic cloud characteristics observed by radar and lidar at SHEBA. *J. Geophys. Res.,* **107(C10),** 8030.

IPCC, 1990: Climate Change: *The IPCC Scientific Assessment.* J. T. Houghton, G. J. Jenkins, and J. J. Ephraums, Eds., Cambridge University Press, 365pp.

Levin, Z., and W. R. Cotton, 2009: Aerosol pollution impact on precipitation: *A scientific review.* Springer Science+Business Media B.V.

Lubin, D., and A. M. Vogelmann, 2006: A climatologically significant aerosol longwave indirect effect in the Arctic. *Nature,* **439,** 453-456.

MacBean, G., 2004: Arctic climate – Past and present. *Impacts of a Warming Arctic: Arctic Climate Impacts Assessment,* S. J. Hassol, Ed., Cambridge University Press, 21-60.

Mahrer, Y., and R. A. Pielke, 1981: Simulations of the effects of surface fluxes of heat and moisture in a mesoscale numerical model. Part I: Soil layer. *J. Geophys. Res.,* **86,** 9929-9938.

Mellor, G. L., and T. Yamada, 1982: Development of a turbulence closure model for geophysical fluid problems. *Rev. Geophys. Space Phys.,* **20,** 851-875.

Meyers, M. P., P. J. DeMott, W. R. Cotton, 1992: New primary ice nucleation parameterizations in an explicit cloud model. *J. Appl. Meteor.,* **31,** 708-721.

Mitchell, D. L., A. Macke, and Y. Liu, 1996: Modeling cirrus clouds. Part II: Treatment of radiative properties. *J. Atmos. Sci.,* **53,** 2967-2988.

Overland, J. E., 1997: Regional variation of winter temperatures in the Arctic. *J. of Climate,* **10,** 821-837.

Pielke, R. A., W. R. Cotton, R. L. Walko, C. J. Tremback, W. A. Lyons, L. D. Grasso, M. E. Nicholls, M. D. Moran, D. A. Wesley, T. J. Lee, and J. H. Copeland, 1992: A comprehensive meteorological modeling system – RAMS. *Meteor. Atmos. Phys.,* **49,** 69-91.

Prenni, A. J., J. Y. Harrington, M. Tjernstrom, P. J. DeMott, A. Avramov, C. N. Long, S. M. Kreidenweis, P. Q. Olsson, and J. Verlinde, 2007: Can ice-nucleating aerosols affect Arctic seasonal climate?, *Bull. Am. Meteor. Soc.,* **88,** 541-550.

Ritter, R. A., and J. F. Geleyn, 1992: A comprehensive radiation scheme for numerical weather prediction models with potential applications in climate simulations. *Mon. Wea. Rev.,* **120,** 303-325.

Rogers, D. C., P. J. DeMott, and S. M. Kreidenweis, 2001: Airborne measurements of tropospheric ice-nucleating aerosol particles in the Arctic spring. *J. Geophys. Res.,* **106,** 15 053-15 063.

Saleeby, S. M., and W. R. Cotton, 2008: A binned approach to cloud-droplet riming implemented in a bulk microphysical model. *J. Appl. Meteor. Clim.,* **47,** 694-703.

Serreze, M., and J. A. Francis, 2006: The Arctic amplification debate. *Climate Dyn.,* **76,** 241-264.

Slingo, A. and M. Schreckner, 1982: On shortwave properties of stratiform water clouds. *Quart. J. Roy. Meteor. Soc.,* **108,** 407-426.

Tremback, C. J., 1990: *Numerical simulation of a mesoscale convective complex: Model development and numerical results*. PhD Diss., Atmos. Sci. Paper No. 465, Colorado State University, Department of Atmospheric Science, Fort Collins, CO 80523.

Tripoli, G. J., and W. R. Cotton, 1982: The Colorado State University three-dimensional cloud/mesoscale model – 1982. Part I: General theoretical framework and sensitivity experiments. *J. Rech. Atmos.,* **16,** 185-220.

Twomey, S., 1977: *Atmospheric Aerosols.* Elsevier, 287-290.

Verlinde, J., P. J. Flatau, and W. R. Cotton, 1990: Analytical solutions to the collection growth equation: Comparison with approximate methods and application to cloud microphysics parameterization schemes. *J. Atmos. Sci.,* **47,** 2871-2880.

Vowinckel, E., 1962: Cloud amount and type over the Arctic. *Publication in Meteorology,* No. 51, pp. 27.

Walko, R. L., C. J. Tremback, R. A. Pielke, and W. R. Cotton, 1995: An interactive nesting algorithm for stretched grids and variable nesting ratios. *J. Appl. Meteo.,* **34,** 994-999.

Walko, R. L., L. E. Band, J. Baron, T. G. F. Kittel, R. Lammers, T. J. Lee, D. Ojima, R. A. Pielke Sr., C. Taylor, C. Tague, C. J. Tremback, and P. J. Vidale, 2000: Coupled atmosphere-biophysics-hydrology models for environmental modeling. *J. Appl. Meteor.,* **39,** 931-944.

Warren, S. G., C. J. Hahn, J. London, R. M. Chervin, and R. L. Jenne, 1988: *Global Distribution of Total Cloud Cover and Cloud Type Amounts over the Ocean.* NCAR/TN-317+STR, 212 pp.

Wu, T., W. R. Cotton, and W. Y. Y. Cheng, 2000: Radiative effects on the diffusional growth of ice particles in cirrus clouds. *J. Atmos. Sci.,* **57,** 2892-2904.